

PREDICTION OF INFRASOUND EMISSION FROM
HORIZONTAL AXIS WIND TURBINES

by

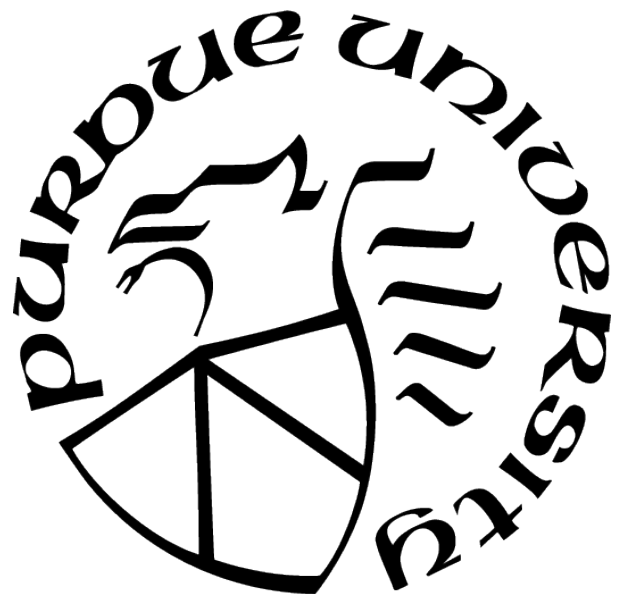
Dazhuang He

A Thesis

Submitted to the Faculty of Purdue University

In Partial Fulfillment of the Requirements for the degree of

Master of Science in Mechanical Engineering



School of Mechanical Engineering

West Lafayette, Indiana

December 2021

THE PURDUE UNIVERSITY GRADUATE SCHOOL
STATEMENT OF COMMITTEE APPROVAL

Dr. Jun Chen, Co-chair

School of Mechanical Engineering

Dr. Yangfan Liu, Co-chair

School of Mechanical Engineering

Dr. J. Stuart Bolton

School of Mechanical Engineering

Dr. Patricia Davies

School of Mechanical Engineering

Approved by:

Nicole L. Key

ACKNOWLEDGMENTS

First of all, I would like to express my sincere gratitude to my advisor Prof. Jun Chen and co-advisor Prof. Yangfan Liu. Their academic experiences, patience and kindness has been of great help through out the years. It would be impossible to finish this thesis without their most needed assistance. I am also thankful for Prof. J. Stuart Bolton and Prof. Patricia Davies' instructions. Their instructions pave the way for me to study an acoustic topic in depth. Their dedications and rigorous altitudes towards academia set great examples for me.

I'd also like to thank other researchers, professors and staff working at Ray W. Herrick Laboratories. They create a friendly and warm working space and I've received many insightful suggestions from my communications with them.

Last but not least, I want to thank my family. They always have confidence in me and keep encouraging me. I wouldn't have finished the work without their support.

TABLE OF CONTENTS

LIST OF TABLES	6
LIST OF FIGURES	7
LIST OF SYMBOLS	9
ABBREVIATIONS	11
ABSTRACT	12
1 INTRODUCTION	13
1.1 Working Principle of Wind Turbine	15
Airfoil and Wind Turbine Aerodynamics	16
Wind Turbine Blade	18
1.2 Wind Farm Control	23
1.3 Environmental Impacts of Wind Turbines	23
2 AERODYNAMIC NOISE FROM WIND TURBINES: LITERATURE REVIEW	26
2.1 Aerodynamic Noise	26
2.1.1 Inhomogeneous Linear Wave Equation	27
2.1.2 Lighthill's Analogy	28
2.1.3 Curle's Theorem	30
2.1.4 FW-H Equation	33
2.1.5 Farassat's Formulation 1 and 1A	34
2.2 Wind Turbine Noise	40
2.2.1 Noise Mechanism	40
Steady thickness and loading noise	41
Noise induced by atmospheric turbulent gust	41
Self-noise of turbine airfoil	43
2.2.2 Prediction Methods for Wind Turbine Noise	44

3 METHODOLOGY	46
3.1 Assumptions	46
3.2 Shape and Pressure Distribution of Wind Turbine Blade	48
3.3 Principle of TDRIP	49
3.3.1 Element and Observer	50
3.3.2 Ground Effect	55
3.4 Validation of Program against CFD	59
4 RESULTS	63
4.1 Infrasound Emitted from Single Turbine	63
4.2 Infrasound Emitted from Two Turbines	71
4.2.1 Wind direction	73
4.2.2 Phase difference	74
5 SUMMARY AND FUTURE WORK	78
5.1 Possible Future Improvement	78
REFERENCES	85

LIST OF TABLES

3.1	Wind Turbine Dimensions	49
3.2	Sphere	59

LIST OF FIGURES

1.1	Ancient panemone windmills at Nishtafun, Iran	13
1.2	(a) The first wind turbine in the US built in 1888 and (b) world's largest wind turbine Vestas V-164	14
1.3	Wind Energy Installed Capacity Trends (From: IRENA [1])	15
1.4	Wind Turbine Components (From: GE [2])	16
1.5	Lift and drag forces acting on a airfoil	17
1.6	Pressure Coefficient Distribution (From: Barbarino <i>et al.</i> [3])	18
1.7	Streamtube surrounding a wind turbine	19
1.8	1-D momentum theory	19
1.9	Maximum power coefficient as a function of tip speed ratio (From: Manwell <i>et al.</i> , 2009 [6])	22
1.10	Meadow Lake wind farm in White County, Indiana	24
2.1	Moving boundary defined by generalized function $H(f)$	31
2.2	Typical Turbulence Energy Spectrum Normalized by Kolmogorov Scale η (From: Pope, 2000 [30])	42
3.1	Methodology	47
3.2	NREL's S816 Airfoil at $\alpha = 0^\circ$	49
3.3	(a) S816 airfoil at $\alpha = 4^\circ$ and (b) pressure coefficient distribution at $\alpha = 4^\circ$	50
3.4	Wind Turbine Schematic	51
3.5	Twist and chord length distributions	52
3.6	Wind Turbine Blade in TDRIP	53
3.7	Observer Time t vs. Source Time τ	54
3.8	Reflection Coefficient and its Impulse Response	56
3.9	Incident wave and reflected wave on ground	57
3.10	Reflection from Ground Surface	58
3.11	(a) sphere surface element and (b) CFD computation domain	60
3.12	Line of Data Points	61
3.13	Thickness Noise Computed using OpenFOAM and TDRIP Program	62
4.1	CFD computation domain	64

4.2	Aerodynamic noise computed by CFD	65
4.3	(a) Turbine Rotor Element in TDRIP Program and (b) Virtual Microphones . .	66
4.4	Time history of aerodynamic noise at different virtual microphones	67
4.5	Fourier coefficient	69
4.6	Directivity pattern of different frequency components	71
4.7	Two turbines configuration	72
4.8	Directivity pattern with different wind angle	74
4.9	Directivity of turbines with phase difference	75
4.10	Time history of wind turbine infrasound emission with phase difference	76
4.11	Four turbines configuration	77
4.12	Directivity of four turbines	77
5.1	(a) Monopole/dipole in circular motion and (b) sound pressure of moving monopole/dipole	80
5.2	Wind turbines siting vs. noise directivity	83
5.3	Computation time of TDRIP program	84

LIST OF SYMBOLS

a	axial induction factor
B	number of blades
C_l	lift coefficient
C_d	drag coefficient
C_p	pressure coefficient
C_P	power coefficient
c_0	speed of sound
D	airfoil drag
D_{rotor}	rotor diameter
f	equation of a surface(only in Section 2.1) or frequency(otherswise)
f_s	sampling frequency
G	Green's function
H	Heaviside function
H_{hub}	hub height
L	airfoil lift
l_c	airfoil chord length
M_r	Mach number of source going towards observer
p, p_0, p'	fluid pressure
R_{mic}	distance between wind turbine and virtual microphone
R_{rotor}	rotor radius
$\hat{R}(f), R(t)$	reflection coefficient
\mathbf{r}, r_i	vector pointing from observer to source
T	rotor thrust
T_0	period of rotation
T_{ij}	Lighthill's stress tensor
t	observer time
\mathbf{U}, U_i	velocity
V_w	wind speed

V_{rel}	relative wind speed
\mathbf{x}, x_i	location of observer/microphone
\mathbf{y}, y_i	location of source
Z_c	normalized specific impedance of ground
α	angle of attack
δ	delta function
δ_{ij}	Kronecker delta
η	coordinates in Lagrangian frame
θ	azimuthal angle
λ	tip speed ratio
λ_a	wavelength of sound wave
ρ, ρ_0, ρ'	fluid density
τ	source time
τ_{ij}	viscous shear tensor
φ	relative wind angle
φ_d	wind turbine phase difference
Ω	angular velocity of rotor

ABBREVIATIONS

AMI	arbitrary mesh interface
BPF	blade passing frequency
CFD	computational fluid dynamics
TDRIP	Time Domain Rotor Infrasound Prediction
DFT/IDFT	Discrete Fourier Transform/Inverse Discrete Fourier Transform
FW-H	Ffowcs Williams and Hawking
HAWT	horizontal axis wind turbine
TSR	tip speed ratio

ABSTRACT

Wind energy is one of the fastest-growing renewable energy technologies, and horizontal axis wind turbines (HAWT) have been the most common device to convert wind kinetic energy into electrical energy. As the capacities of wind turbines and scales of wind farm constructions are rapidly increasing over time, environmental impacts of wind energy are becoming more relevant and raising more attention than ever before. One of the major environmental concerns is noise emission from wind energy facilities, especially low-frequency noise and infrasound that allegedly cause so-called wind turbine syndrome. Therefore, a numerical simulation program capable to predict low-frequency noise and infrasound emission from wind turbines is a useful tool to aid future wind energy development. In this study of this thesis, a computer program named TDRIP (Time Domain Rotor Infrasound Prediction) is developed based on acoustic analogy theories. Farassat's formulation 1A, a solution to Ffowcs Williams-Hawkins (FW-H) equation, is implemented in the TDRIP program to compute aerodynamically generated sound. The advantage of this program is its capability to simultaneously compute infrasound emission of multiple wind turbines in time domain, which is a challenging task for other aerodynamic noise prediction methods. The developed program is validated against results obtained from computational fluid dynamics (CFD) simulations. The program is then used to compute aerodynamic noise emitted from wind turbine rotors. The effects of wind direction, wind turbine siting, and phase of wind turbine rotation on consequent aerodynamic noise are investigated. Results of aerodynamic noise computation imply that wind turbine siting configuration or wind turbine phase adjustment can help reducing noise level at certain locations, which make the program ideal to be integrated into wind farm siting or control tools.

1. INTRODUCTION

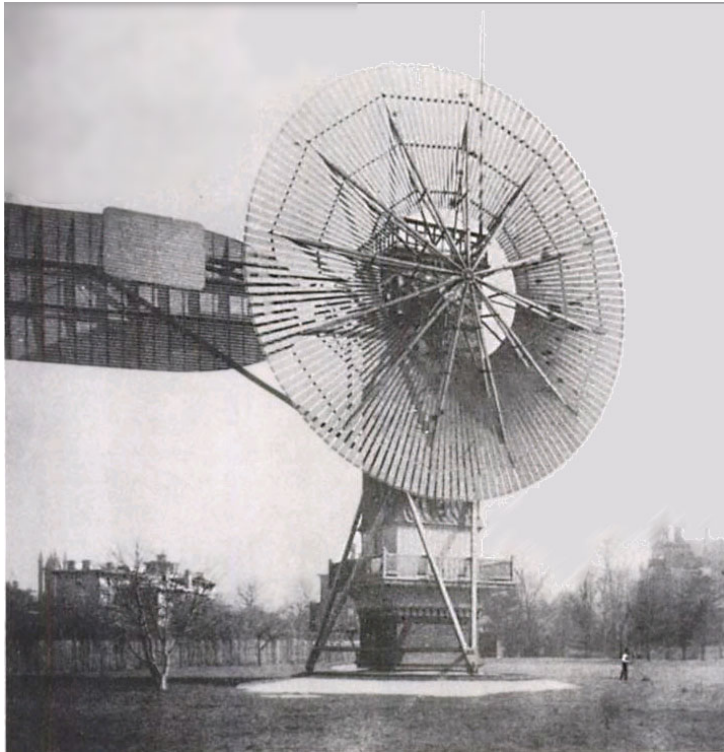
The utilization of wind energy can be dated back to the 9th century when Persian people built panemone windmills (Fig. 1.1). Panemone windmills are vertical axis windmills and they are driven by a drag force, unlike the later horizontal-axis windmills that are driven by lift force. horizontal-axis windmills started appearing in Europe in the 12th century and they gradually got popularity across the continent. By the 14th century, horizontal-axis windmills are widely used in Netherlands for both food production and marsh draining. In 1850, the estimated number of installed windmills in Europe was 200,000. However, with the emerge of the industrial revolution, steam and internal combustion engines replaced windmills for many applications, and the use of wind energy thus declined.



Figure 1.1. Ancient panemone windmills at Nishtafun, Iran

With the increasing demand for electricity, modern wind turbines with electric generators first emerged in the late 19th century. Following the invention of the electric generator in the 1830s, engineers started attempting to harness wind energy to produce electricity. Wind power generation took place in the United Kingdom and the United States in 1887 and 1888 (Fig.1.2a), but modern wind power is considered to have been first developed in Denmark, where horizontal-axis wind turbines (HAWT) were built in 1891 and a 22.8-meter wind turbine began operation in 1897.

In spite of a humble beginning, wind turbine capacities have increased rapidly over time. In 1985, typical turbines had a rated capacity of 0.05 MW and a rotor diameter of 15 meters. Today's commercially available wind turbines have reached 8 MW capacity, with



(a)



(b)

Figure 1.2. (a) The first wind turbine in the US built in 1888 and (b) world's largest wind turbine Vestas V-164

rotor diameters of up to 164 meters (Fig.1.2b). The average capacity of wind turbines increased from 1.6 MW in 2009 to 2 MW in 2014.

Wind power is one of the fastest-growing renewable energy technologies. Usage is on the rise worldwide, in part because costs are falling. Globally, installed wind energy capacity onshore and offshore has increased by a factor of 43 in the past two decades, jumping from 17 gigawatts in 2000 to some 733 gigawatts by 2020, according to the latest data provided by International Renewable Energy Agency (IRENA) [1]. Production of wind electricity doubled between 2009 and 2013, and in 2016 wind energy accounted for 16% of the electricity generated by renewables. Many parts of the world have strong wind speeds, but the best locations for generating wind power are sometimes remote ones. Offshore wind power offers tremendous potential.

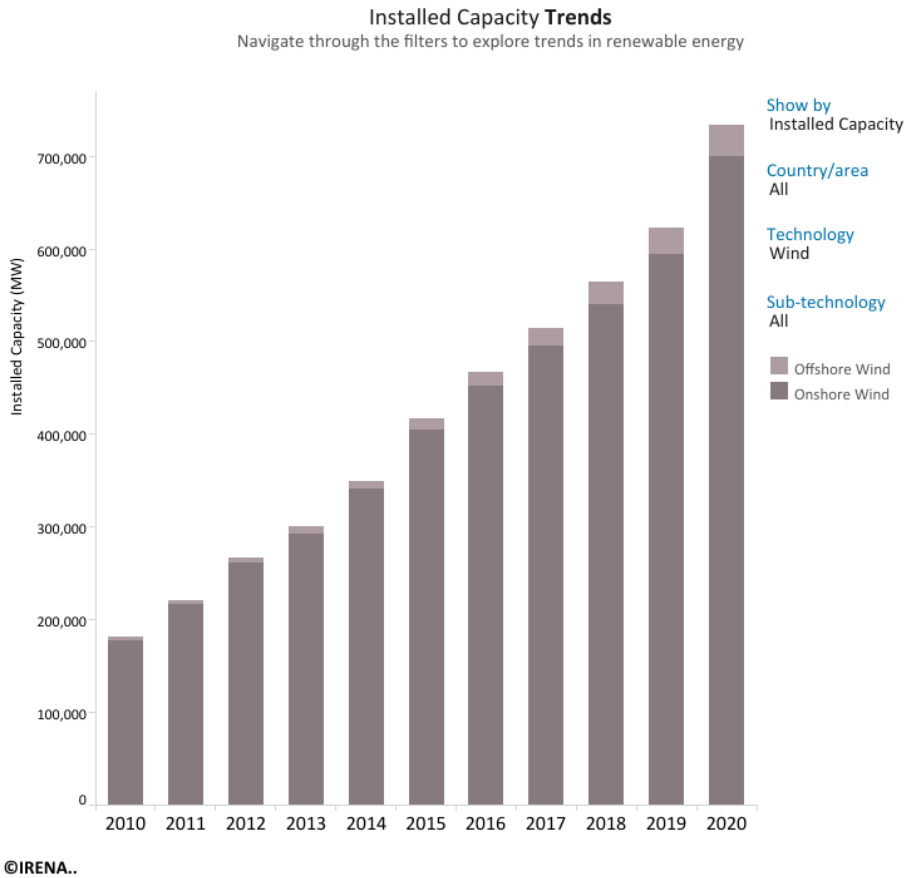


Figure 1.3. Wind Energy Installed Capacity Trends (From: IRENA [1])

1.1 Working Principle of Wind Turbine

Wind turbines are rotary machines that convert the kinetic energy of atmospheric air flow into electricity. Today, the most commonly installed wind turbines are upwind horizontal-axis wind turbines (HAWT), and this specific configuration of a wind turbine is the subject of this thesis. An upwind wind turbine consists of the following major components:

- Rotor, including blades and hub
- Drive train, including shaft, gearbox, coupling, and generator
- Nacelle and tower that houses the drive train, controller, and yaw drive
- Electrical system

The typical structure of a modern upwind HAWT is shown in Figure 1.4. In principle, the turbine is driven by the lift force generated from the blades. The purpose of yaw drive is to guarantee that the plane of turbine rotation is perpendicular to the wind direction. The pitch control guarantees optimal pitch angle of blades, where the lift-to-drag ratio is high.

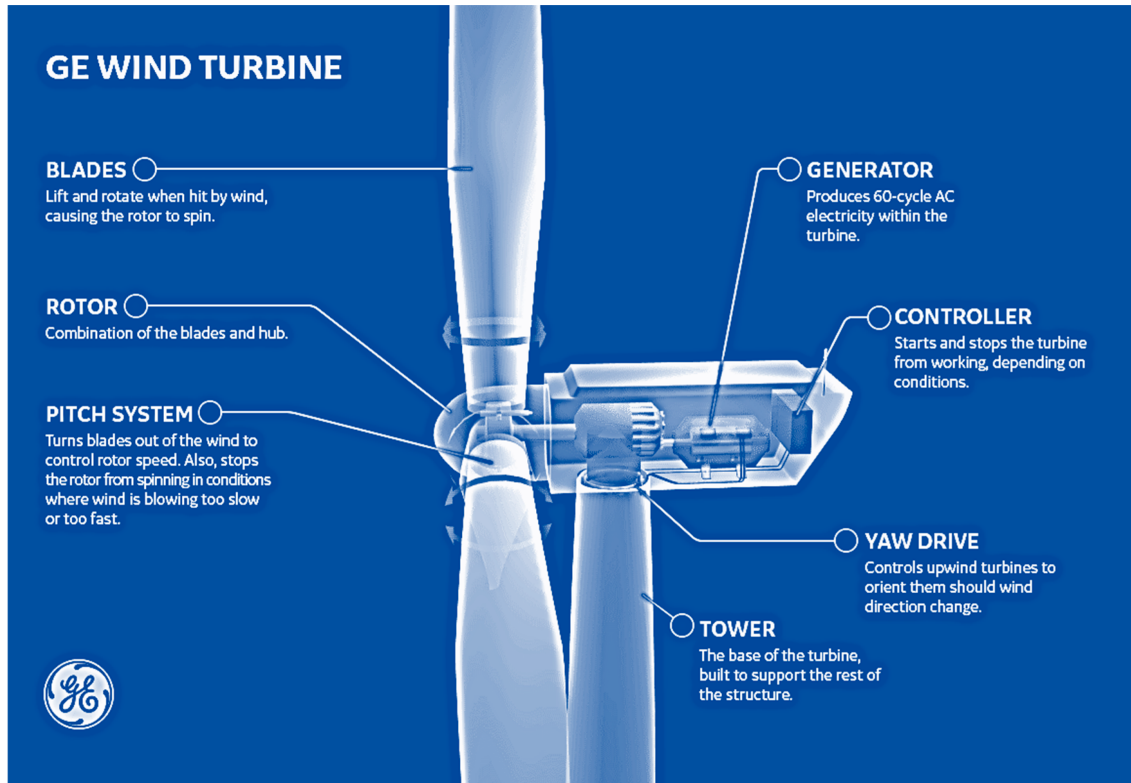


Figure 1.4. Wind Turbine Components (From: GE [2])

Airfoil and Wind Turbine Aerodynamics

Airfoils are structures with specific geometric shapes that are used to generate mechanical forces due to the relative motion of the airfoil to the surrounding fluid. Wind turbine blades are driven by the lift force on airfoils. Before introducing the acoustics aspect of wind turbines, the aerodynamics aspects related to airfoil need to be discussed.

Some concepts related to airfoil are shown in Figure 1.5. The most forward and rearward points of the airfoil are on the leading edge and trailing edge respectively. The straight line connecting the leading edge and trailing edge is the chord line of the airfoil, and the length

of the chord line is designated l_c . The angle of attack α is defined as the angle between wind velocity V_{rel} direction and the chord line.

The surrounding fluid exerts force on an airfoil. The resultant of forces on airfoil surface is usually decomposed into two directions - perpendicular and parallel to wind direction. The component perpendicular to wind direction is called lift force and the component parallel to wind direction is called drag force. The non-dimensional lift and drag forces are so-called lift coefficient C_l and drag coefficient C_d , defined as

$$C_l = \frac{L}{\frac{1}{2}\rho U^2 l_c}, \quad (1.1)$$

$$C_d = \frac{D}{\frac{1}{2}\rho U^2 l_c},$$

where L and D are lift and drag forces per unit length of blade and $\frac{1}{2}\rho U^2$ is the dynamic pressure of incoming air flow.

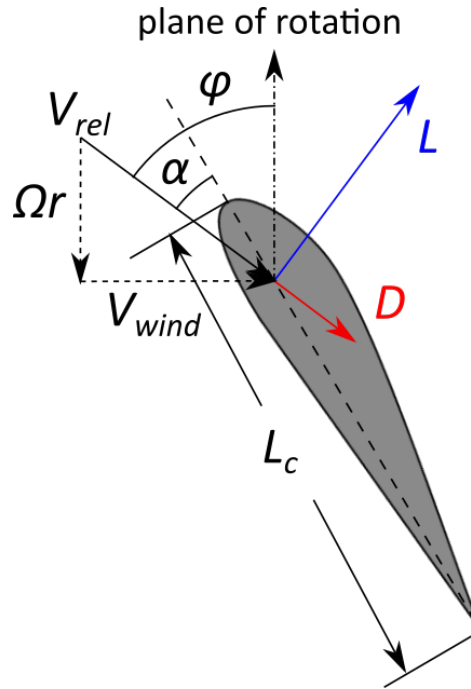


Figure 1.5. Lift and drag forces acting on a airfoil

Pressure coefficient C_p is another important dimensionless coefficient, which is defined as

$$C_p = \frac{p - p_\infty}{\frac{1}{2}\rho U^2}, \quad (1.2)$$

where $p - p_\infty$ is static pressure on a certain point on airfoil. A typical pressure coefficient distribution along airfoil surface is shown in Figure 1.6.

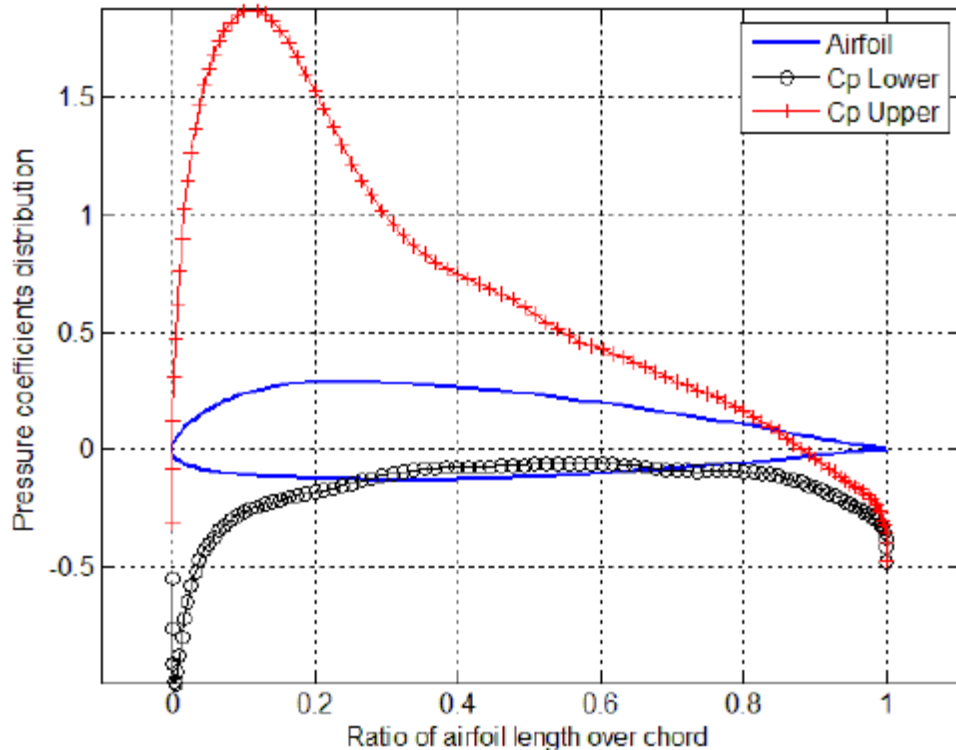


Figure 1.6. Pressure Coefficient Distribution (From: Barbarino *et al.* [3])

Wind Turbine Blade

Wind turbines are machines that harvest wind energy. The amount of power that can be harvested from wind depends on the size of the turbine and the length of its blades. The output is proportional to the dimensions of the rotor and to the cube of the wind speed. Theoretically, when wind speed doubles, wind power potential increases by a factor of eight. The theory that relates the aerodynamics of a turbine and the amount of power it can harvest from wind was initially established by Betz [4].

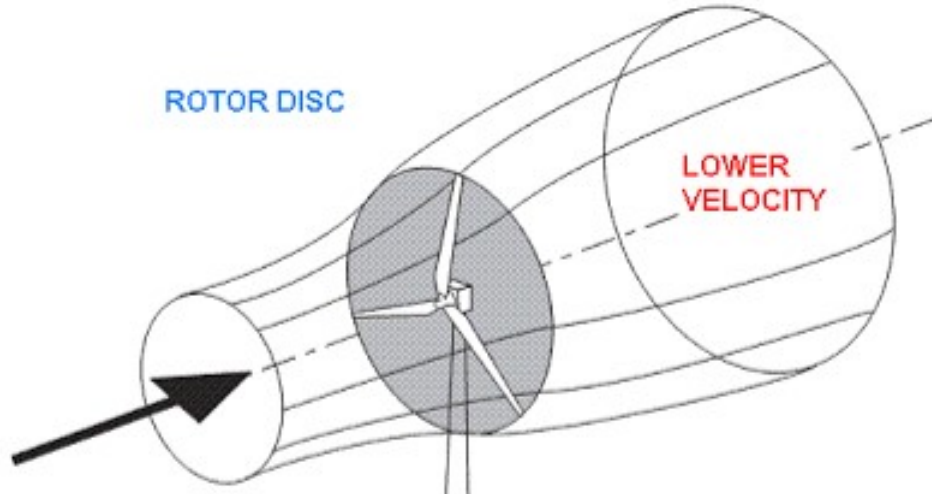


Figure 1.7. Streamtube surrounding a wind turbine

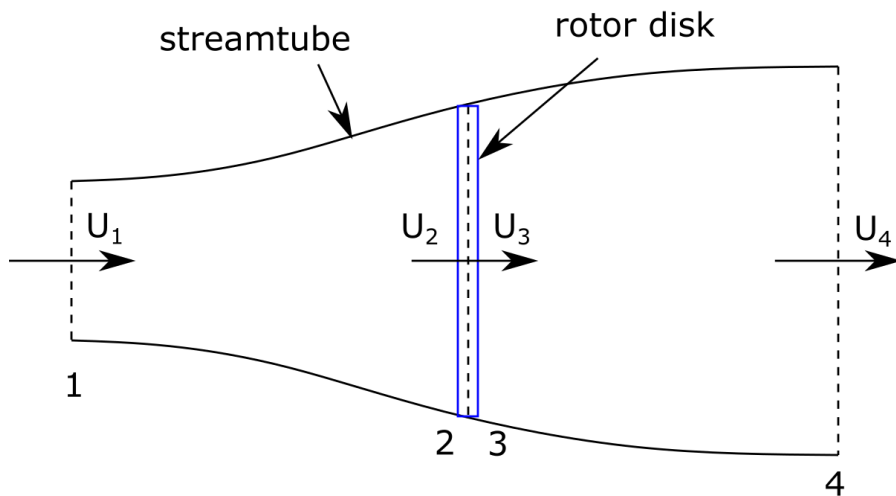


Figure 1.8. 1-D momentum theory

Betz's model is based on one-dimensional control volume analysis of momentum. In Betz's model, it's assumed that the flow is steady, incompressible, and inviscid, the rotational wake (flow angular momentum) is neglected and thrust force is uniformly distributed on the rotor disk. In addition, it's also assumed that the velocity is continuous across the rotor and the fluid pressure at far upwind and downwind locations are the same, which means $U_2 = U_3$ and $p_1 = p_4$ in Figure 1.8.

By using conservation of mass and momentum of the control volume (Fig. 1.8), the thrust applied on the rotor disk can be expressed as

$$T = \dot{m}(U_1 - U_4), \quad (1.3)$$

where T is thrust force, \dot{m} is mass flow rate of streamtube, U_1 and U_4 are velocity at section 1 and 4 respectively. U_1 represents free stream wind speed, which will also be denoted with V_w later. Thrust of rotor disk can also be expressed in terms of the pressure difference across the disk as

$$T = A_2(p_2 - p_3). \quad (1.4)$$

Equation 1.4 can be reduced by using Bernoulli's equation, so that thrust T can be expressed in terms of velocity as

$$T = \frac{1}{2}\rho A_2(U_1^2 - U_4^2). \quad (1.5)$$

Expression of wind turbine power P can be thus derived as thrust times velocity as

$$P = TU_2 = \frac{1}{2}\rho A_2(U_1^2 - U_4^2)U_2. \quad (1.6)$$

It's desirable to relate power P with upstream wind speed U_1 . For that purpose, axial induction factor a is defined as:

$$a = \frac{U_1 - U_2}{U_1}. \quad (1.7)$$

Now that there are two equations of thrust (Eq. 1.3 and Eq. 1.4), by equating these equations, a velocity relation can be obtained as

$$U_2 = \frac{U_1 + U_4}{2}. \quad (1.8)$$

With Equation 1.7 and 1.8, velocity at any section can be expressed in terms of free stream velocity U_1 and axial induction factor a as

$$\begin{aligned} U_2 &= U_1(1 - a), \\ U_4 &= U_1(1 - 2a), \end{aligned} \quad (1.9)$$

so that power P can be expressed in terms of upstream wind speed U_1 , rotor disk area A_2 and axial induction factor a as

$$P = 2\rho A_2 U_1^3 a(1 - a)^2. \quad (1.10)$$

Power coefficient, a dimensionless coefficient that implies the fraction of power harvested by a wind turbine, is defined as

$$C_P = \frac{P}{\frac{1}{2}\rho A_2 U_1^3} = 4a(1 - a)^2. \quad (1.11)$$

Power coefficient C_P is a cubic function of a and it is maximized at $a = 1/3$, $C_P = 16/27 \approx 0.5926$. This is the theoretically maximum performance limit of wind turbines and the later analysis is based on this conclusion. C_P of actual wind turbines is lower than the max limit because of the rotational wake behind the wind turbine, frictions, and other mechanisms of momentum loss.

When rotational wake is considered, an analysis with angular momentum can be carried out in similar manners [5]. The analysis shows that the maximum power coefficient of a wind turbine is a function of tip speed ratio (TSR) [6] (Fig. 1.9), a parameter defined as

$$\lambda = \frac{\Omega R}{V_w}, \quad (1.12)$$

where Ω and R are angular velocity and radius of the rotor. From Figure 1.9, the maximum power coefficient is very close to the limit of Betz's theory when $\lambda > 5$. TSR of modern large onshore wind turbines can reach 7 or even higher ($\lambda = 7.5$ for GE 6 MW model, for example), which makes their performance close to the ideal wind turbine of Betz's model.

It's obvious that the relative wind speed $V_{rel} = \frac{2U_1}{3\sin\varphi}$ is different on different spanwise locations along a wind turbine blade. When considering the design of a wind turbine blade, it's necessary to analyze an infinitesimal spanwise section of the blade. The infinitesimal lift of a section is

$$dL = Cl \frac{1}{2} \rho V_{rel}^2 dr. \quad (1.13)$$

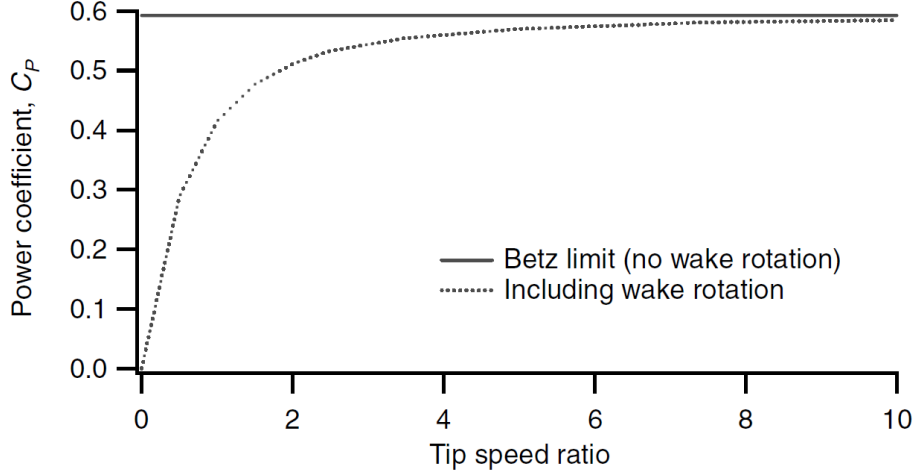


Figure 1.9. Maximum power coefficient as a function of tip speed ratio (From: Manwell *et al.*, 2009 [6])

Therefore the infinitesimal thrust force of all the sections on a certain radius is

$$dT = BdL \cos \varphi, \quad (1.14)$$

where B is the number of blades of a wind turbine. On the other hand, from Equation 1.3 and 1.7, infinitesimal thrust force at certain radius is

$$dT = \frac{8}{9} \rho V_w^2 \pi r dr, \quad (1.15)$$

where wind speed $V_w = U_1$. By equating two expressions of dT (Equations 1.14 and 1.15), the relation between rotor radius r and angle φ can be obtained as

$$\begin{aligned} \frac{C_l Bl_c}{4\pi r} &= \tan \varphi \sin \varphi, \\ \tan \varphi &= \frac{U_2}{\Omega r} = \frac{2V_w}{3\Omega r}. \end{aligned} \quad (1.16)$$

Equation 1.16 relates lift coefficient C_l , chord length l_c and relative wind angle φ with certain radial location r of a wind turbine. This equation will be the cornerstone of blade design. The process of blade design using Equation 1.16 will be shown in Chapter 3.

1.2 Wind Farm Control

A wind farm is a group of wind farms at the same location that provides bulk power to the electrical grid. The world's first wind farm was installed in Crotched Mountain in New Hampshire, consisting of twenty 30 kW wind turbines. To this date, the Gansu wind farm, the world's largest wind farm, consists of more than 7000 wind turbines and has a total capacity of 8000 MW. As the number of wind turbines in a wind farm grows rapidly, the coordination of wind farms becomes significant, so that the control of wind farms emerges as a new area of research. There are three major objectives of wind farm control [7]: (i) Maximize active power of a wind farm, (ii) Follow a reference for wind farm active power, and (iii) Minimize fatigue loads while maintaining the power.

In a wind farm, each wind turbine is affected by the wake of other upstream wind turbines. For the purpose of wind farm control, the wake effect is either simply modeled as done by Katic *et al.* [8], or modeled based on CFD as done by Fleming *et al.* [9]. The control of wind farms with wake effects has been extensively studied for more than 20 years [10]. However, there hasn't been a study of wind farm control with consideration of noise emission. The sound emitted from each individual wind turbine can interfere with the sound emitted from other wind turbines, which leads to a conceptually similar interaction as wake flow interactions between wind turbines. A sound emission assessing model for wind turbines can possibly envision wind farm control strategies that account for wind farm noise emission.

1.3 Environmental Impacts of Wind Turbines

The impact of wind turbines on wildlife, most notably on birds and bats, has been widely documented and studied. A National Wind Coordinating Committee (NWCC) review of peer-reviewed research found evidence of bird and bat deaths from collisions with wind turbines and due to changes in air pressure caused by the spinning turbines [11]. The NWCC concluded that these impacts are relatively low and do not pose a threat to species populations

Sound is the main public health and community concern associated with operating wind turbines. Most of the sound generated by wind turbines is aerodynamic, caused by the



Figure 1.10. Meadow Lake wind farm in White County, Indiana

movement of turbine blades through the air. Overall sound levels depend on turbine design and wind speed. There has been a contradiction of whether the aerodynamic sound generated from wind turbine operation causes adverse health effects. On the one hand, some people living close to wind facilities have reported annoyance, stress, sleep disturbance, headache, anxiety, depression, and cognitive dysfunction [12]. On the other hand, there are also studies that imply there is no statistically significant evidence of human health impacts from wind turbines [13]. Schmidt and Klokker reviewed comprehensive studies related to the health effects related to wind turbine noise exposure [14], and they concluded that noise from wind turbines increased the risk of annoyance and disturbed sleep in exposed subjects in a dose-response relationship and suggested a cautious approach when planning future wind farms.

Infrasound is the sound of frequency below 20 Hz and is considered inaudible. The possible health effect caused by infrasound exposure is a debatable topic. Some medical researches revealed potential psychological effects of infrasound exposure [15]. The blade passing frequency (BPF) of a modern large onshore wind turbine (>2 megawatts) is well below 20 Hz. Therefore the air disturbances caused by wind turbine operation of such wind turbine can be considered as infrasound emission. van den Berg's sound measurement result

for a single wind turbine confirmed that the (unweighted) sound level is highest at infrasound frequency range [16].

Even though the infrasound emitted from wind turbines is not directly audible, it's still believed to be one of the reasons for annoyance. The low-frequency noise can well excite building structures, such as walls, floors and windows [17]. It has been reported that "some people feel disturbing amounts of vibration or pulsation from wind turbines, and can count in their bodies, especially their chests, the beats of the blades passing the towers, even when they can't hear or see them." [18] Such annoyances and disturbances caused by wind turbines are categorized into so-called *wind turbine syndrome*.

With actual public health concerns, reduction of potential health risk from sound has become a siting criterion for wind farms. Kamperman and James proposed siting criteria of wind farms based on single turbine sound measurement results [19]. However, the single turbine measurement cannot be used to predict possible sound interference of multiple turbines, as implied by van den Berg's measurement results [20]. Therefore, it's desirable to develop a tool capable to predict sound and infrasound emissions from wind turbines. Such a tool can help to address the public health concerns associated with wind turbine operation and developing guidelines for wind turbine siting oriented by noise emission, and this is the major motive of this thesis. The next question would be how to develop such a tool. In the next chapter, related literature will be reviewed to lay the theoretical foundation for the development of wind turbine prediction tools.

2. AERODYNAMIC NOISE FROM WIND TURBINES: LITERATURE REVIEW

In the first chapter, the development of wind energy is briefly introduced, together with environmental concerns raised by wind energy development. One of the major environmental impacts is the aerodynamic noise emitted from wind turbines and therefore it's motivating to develop an aerodynamic noise prediction tool. In this chapter, aerodynamic noise theories are to be reviewed and the development of aerodynamic noise theories are to be followed, from its origin to mathematical formulations that are ready to be implemented in computer programs, so that a solid foundation is laid for the development of the wind turbine noise prediction tool.

2.1 Aerodynamic Noise

Gutin pioneered the study of aerodynamic noise in 1936 [21] by theoretically investigating the relationship between the thrust/torque of a propeller and the generated aerodynamic noise at its blade passing frequency (BPF). He integrated the fluid velocity potential disturbance induced by aerodynamic forces over a propeller blade and correctly predicted the directivity pattern of the blade passage tone of propeller aerodynamic noise.

In 1952, Lighthill introduced the theory now known as acoustics analogy in his study of jet noise [22]. Sound is generated when the fluid medium is perturbed. In traditional acoustics studies, the perturbation can be mathematically expressed in terms of boundary conditions. However, with the invention of the jet engine in the 1940s, it was realized that the traditional theory cannot explain the generation of jet noise. When high-speed jet flow is injected into stationary fluid, fluid shearing causes strongly turbulent flow and strong noise is generated consequently. The generation of jet noise does not involve perturbations that can be explicitly expressed. Instead, jet noise is generated from non-linear fluid interactions. Lighthill, by reformulating the continuity and momentum equation of fluid motion, included the effects of non-linear fluid interactions in the source term of a linear wave equation. The equation indicated that the noise radiation from a turbulent gust was as if it were a quadrupole. The equation reduces to a linear wave equation outside the region where turbulent flow interaction

occurs and describes the noise radiation outside the turbulent flow region. Lighthill further carried out a dimensional analysis of aerodynamic sound production and he found that the intensity of jet noise scaled with the eighth power of jet speed.

In 1955, Lighthill's theory was extended by Curle to incorporate the effect of solid boundaries [23]. By solving Lighthill's wave equation, it was found that the effects of solid boundaries are equivalent to dipoles distributed on the boundary, representing loads exerted upon fluids by solid boundaries. A dimensional analysis showed that flow-induced dipoles contributed more to the sound field than flow-induced quadrupoles.

In 1969, Ffowcs Williams and Hawking developed powerful techniques to include arbitrary motions of solid boundaries in Lighthill-Curle's theory of aerodynamic noise [24]. Their idea was to use generalized functions to extend the definition of medium properties across solid boundaries. One of the difficulties in Curle's theory was finding the Green's function that accommodated solid boundaries. In the theory developed by Ffowcs Williams and Hawking, free-space Green's function can be used regardless, with the help of generalized function. Farassat put forward the solution of Ffowcs Williams and Hawking equation in different forms, namely, Formulation 1 and Formulation 1A, that can be conveniently implemented in nowadays computational acoustic analysis software [25][26].

In the following subsections, the complete mathematical derivation of acoustic analogy theories will be shown. It will start with fundamental fluid mechanics, and it will eventually reach the formulations that can be directly evaluated in a computer program developed by the author of the thesis.

2.1.1 Inhomogeneous Linear Wave Equation

Theories of acoustic analogy often yield inhomogeneous wave equations (wave equation with source terms). Such equations can be directly derived from equations of fluid motion, and the process will be demonstrated. The content of this subsection is not directly related to aerodynamic noise theories, but it helps understanding where different types of source terms come from.

The velocity field $u_i(\mathbf{x}, t)$ and pressure field $p(\mathbf{x}, t)$ of an inviscid flow can be described by the continuity equation and momentum equation

$$\begin{aligned}\frac{\partial \rho}{\partial t} + \frac{\partial}{\partial x_i}(\rho u_i) &= \rho q, \\ \frac{\partial}{\partial t}(\rho u_i) + \frac{\partial}{\partial x_j}(\rho u_i u_j) &= -\frac{\partial p}{\partial x_i} + F_i,\end{aligned}\tag{2.1}$$

where q and F_i are the volume source and volume force per unit volume.

Equations 2.1 can be linearized, if small perturbations of pressure and density are assumed, i.e., $p' = p - p_0 \ll p_0$ and $\rho' = \rho - \rho_0 \ll \rho_0$ where p_0 and ρ_0 are stationary and uniform mean pressure and density), yielding the linearized continuity equation and the linearized momentum equation:

$$\begin{aligned}\frac{1}{\rho_0} \frac{\partial}{\partial t}(\rho - \rho_0) + \frac{\partial u_i}{\partial x_i} &= q, \\ \rho_0 \frac{\partial u_i}{\partial t} + \frac{\partial}{\partial x_i}(p - p_0) &= F_i.\end{aligned}\tag{2.2}$$

Furthermore, when ρ' and p' represent acoustic perturbations, assuming adiabatic thermodynamic process will give $(p - p_0) = c_0^2(\rho - \rho_0)$, where c_0 is the speed of sound. u_i can be then eliminated:

$$\left(\frac{\partial^2}{\partial t^2} - c_0^2 \frac{\partial^2}{\partial x_i \partial x_i} \right) (\rho - \rho_0) = \rho_0 \frac{\partial q}{\partial t} - \frac{\partial F_i}{\partial x_i}.\tag{2.3}$$

Equation 2.3 is the inhomogeneous wave equation in which the only unknown is the acoustic density fluctuation ($\rho' = \rho - \rho_0$). The two source terms on the right-hand side, with the fluid volume source q and loading F_i , are usually referred to as the monopole source and the dipole source respectively.

2.1.2 Lighthill's Analogy

Lighthill extended the aforementioned equations for inviscid fluid to viscous fluid, starting from the continuity equation

$$\frac{\partial \rho}{\partial t} + \frac{\partial}{\partial x_i}(\rho u_i) = 0\tag{2.4}$$

and the momentum equation

$$\frac{\partial}{\partial t}(\rho u_i) + \frac{\partial}{\partial x_j}(\rho u_i u_j) = \frac{\partial}{\partial x_j}(-p\delta_{ij} + \tau_{ij}), \quad (2.5)$$

where τ_{ij} is viscous stress tensor. By taking the time derivative of equation 2.4 and gradient of equation 2.5 and then subtracting one from another, ρu_i can be eliminated, yielding

$$\frac{\partial^2 \rho}{\partial t^2} = \frac{\partial^2}{\partial x_i \partial x_j}(\rho u_i u_j + p\delta_{ij} - \tau_{ij}). \quad (2.6)$$

A wave equation is then obtained by subtracting $c_0^2 \frac{\partial^2(\rho\delta_{ij})}{\partial x_i \partial x_j}$ from both sides of equation 2.6:

$$\frac{\partial^2 \rho}{\partial t^2} - c_0^2 \frac{\partial^2 \rho}{\partial x_i \partial x_i} = \frac{\partial^2}{\partial x_i \partial x_j}[\rho u_i u_j + (p - c_0^2 \rho)\delta_{ij} - \tau_{ij}]. \quad (2.7)$$

It should be noted that the time derivatives and gradients of p_0 and ρ_0 are zero, so Lighthill's equation is obtained:

$$\begin{aligned} \left(\frac{\partial^2}{\partial t^2} - c_0^2 \frac{\partial^2}{\partial x_i \partial x_i} \right) (\rho - \rho_0) &= \frac{\partial^2}{\partial x_i \partial x_j}[\rho u_i u_j + ((p - p_0) - c_0^2(\rho - \rho_0))\delta_{ij} - \tau_{ij}] \\ &= \frac{\partial^2 T_{ij}}{\partial x_i \partial x_j}, \end{aligned} \quad (2.8)$$

where the Lighthill's stress tensor is $T_{ij} = \rho u_i u_j + ((p - p_0) - c_0^2(\rho - \rho_0))\delta_{ij} - \tau_{ij}$. Equation 2.8 has a form similar to that of Equation 2.3, whereas it is a mere rearrangement of governing equation of fluids without making any further assumption but with more complicated source terms. T_{ij} in source term includes all the non-linear fluid interactions that eventually induce sound, representing a quadrupole type of source. The merit of equation 2.8 lies in that it becomes homogeneous wave equation outside the source region, so it essentially describes the propagation of sound wave outside source region. The propagation of the sound behaves as if it were emitted from acoustic quadrupoles, even though the aerodynamic sound generation involves complicated nonlinear fluid interactions. In other words, the sound generated aerodynamically is analogous to that emitted from acoustic quadrupoles. For this reason the theory developed by Lighthill was named acoustic analogy theory.

Equation 2.8 can be further simplified. Outside the source region, because the propagating acoustic perturbation is adiabatic and small in magnitude, density and pressure perturbation can be related as $(p - p_0) = c_0^2(\rho - \rho_0)$. Additionally, the magnitude of Reynolds stress term $\rho u_i u_j$ is usually much greater than that of viscous stress τ_{ij} . Therefore Equation 2.8 can be simplified as

$$\left(\frac{\partial^2}{\partial t^2} - c_0^2 \frac{\partial^2}{\partial x_i \partial x_i} \right) (\rho - \rho_0) = \frac{\partial^2}{\partial x_i \partial x_j} (\rho u_i u_j). \quad (2.9)$$

2.1.3 Curle's Theorem

Curle's theorem is a development of Lighthill's analogy, which takes the effect of stationary boundaries into account. Assume the boundary is defined by $f(\mathbf{x}) = 0$ (One is noted that only in Section 2.1 f indicates the boundary surface while in other sections f refers to frequency.) The Heaviside Step Function

$$H(f(x_i)) = \begin{cases} 1 & \text{for } x_i \text{ enclosed by surface } f = 0 \\ 0 & \text{for } x_i \text{ outside surface } f = 0 \end{cases} \quad (2.10)$$

is introduced to overcome the discontinuity across solid boundaries (Fig. 2.1). So the solution of Lighthill's equation can be formulated in terms of free-space Green's function of wave equation, with the presence of solid boundaries.

An important identity regarding function $H(f)$ is

$$\int_{V(\mathbf{y})} \phi(\mathbf{y}) \nabla H dV(\mathbf{y}) = \oint_{S(\mathbf{y})} \phi(\mathbf{y}) \mathbf{n} dS(\mathbf{y}). \quad (2.11)$$

This identity will be used to convert an integral over the entire space into a finite surface integral. The identity can be directly derived from the fact that the gradient of the Heaviside function is the Dirac delta function.

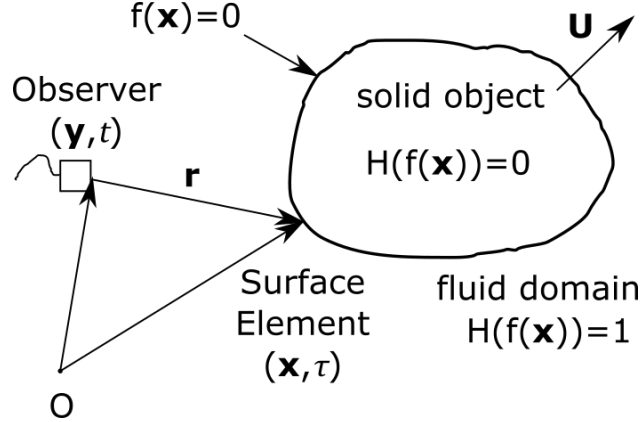


Figure 2.1. Moving boundary defined by generalized function $H(f)$

Next, rearranging the momentum equation in Equation 2.1 to set T_{ij} on the right-hand side yields

$$\frac{\partial}{\partial t} (\rho u_i) + \frac{\partial}{\partial x_i} [c_0^2(\rho - \rho_0)] = -\frac{\partial}{\partial x_j} [\rho u_i u_j + \delta_{ij}((p - p_0) - c_0^2(\rho - \rho_0)) - \tau_{ij}] = -\frac{\partial T_{ij}}{\partial x_j}. \quad (2.12)$$

Multiplying $H(f)$ to Equation 2.12, rearrange such that $H(f)$ appears in the variables

$$\frac{\partial}{\partial t} (\rho u_i H) + \frac{\partial}{\partial x_i} [c_0^2(\rho - \rho_0)H] = -\frac{\partial(T_{ij}H)}{\partial x_j} + [\rho u_i u_j + (p - p_0)\delta_{ij} - \tau_{ij}] \frac{\partial H}{\partial x_j}. \quad (2.13)$$

With similar rearrangement to continuity equation, the following equation can be obtained

$$\frac{\partial}{\partial t} ((\rho - \rho_0)H) + \frac{\partial}{\partial x_i} (\rho u_i H) = \rho u_i \frac{\partial H}{\partial x_i}. \quad (2.14)$$

By taking the time derivative of equation 2.14 and gradient of equation 2.13 and subtracting one from another, an inhomogeneous wave equation is obtained

$$\begin{aligned} \left(\frac{\partial^2}{\partial t^2} - c_0^2 \frac{\partial^2}{\partial x_i \partial x_i} \right) [(\rho - \rho_0)H] &= \frac{\partial}{\partial t} \left(\rho u_i \frac{\partial H}{\partial x_i} \right) \\ &\quad - \frac{\partial}{\partial x_i} \left[(\rho u_i u_j + (p - p_0)\delta_{ij} - \tau_{ij}) \frac{\partial H}{\partial x_j} \right] + \frac{\partial^2}{\partial x_i \partial x_j} (T_{ij}H). \end{aligned} \quad (2.15)$$

With the help of generalized function $H(f)$, Equation 2.15 is a inhomogeneous wave equation defined for all x_i . Then free-space Green's function can be used to solve this inhomogeneous wave equation. For a general inhomogeneous wave equation:

$$\left(\frac{1}{c_0^2} \frac{\partial^2}{\partial t^2} - \frac{\partial^2}{\partial x_i \partial x_i} \right) p = F(t, \mathbf{x}), \quad (2.16)$$

the Green's function $G(\mathbf{x}, t)$ statisfies

$$\left(\frac{1}{c_0^2} \frac{\partial^2}{\partial t^2} - \frac{\partial^2}{\partial x_i \partial x_i} \right) G = \delta(\mathbf{x} - \mathbf{y}) \delta(t - \tau),$$

where \mathbf{x} and t are the observer location and time, \mathbf{y} and τ are source coordinate and time, $\delta(\cdot)$ is Dirac delta function. The free-space Green's fuction for wave equation is:

$$G = \frac{1}{4\pi|\mathbf{x} - \mathbf{y}|} \delta \left(t - \tau - \frac{|\mathbf{x} - \mathbf{y}|}{c_0} \right).$$

With the aid of the Green's function, the general solution to Equation 2.16 can be formulated as

$$p(\mathbf{x}, t) = \frac{1}{4\pi} \int_V \frac{F(\mathbf{y}, t - \frac{|\mathbf{x}-\mathbf{y}|}{c_0})}{|\mathbf{x} - \mathbf{y}|} dV(\mathbf{y}). \quad (2.17)$$

By replacing F in this general solution with source terms in Equation 2.15, one may obtain the solution of Equation 2.15

$$\begin{aligned} c_0^2(\rho - \rho_0)H &= \frac{\partial}{\partial t} \int_S [\rho u_j]_{\tau=t-|\mathbf{x}-\mathbf{y}|/c_0} \frac{n_j dS(\mathbf{y})}{4\pi|\mathbf{x} - \mathbf{y}|} \\ &\quad - \frac{\partial}{\partial x_i} \int_S [\rho u_i u_j + (p - p_0) \delta_{ij} - \tau_{ij}]_{\tau=t-|\mathbf{x}-\mathbf{y}|/c_0} \frac{n_j dS(\mathbf{y})}{4\pi|\mathbf{x} - \mathbf{y}|} \\ &\quad + \frac{\partial^2}{\partial x_i \partial x_j} \int_V [T_{ij}]_{\tau=t-|\mathbf{x}-\mathbf{y}|/c_0} \frac{dV(\mathbf{y})}{4\pi|\mathbf{x} - \mathbf{y}|}. \end{aligned} \quad (2.18)$$

Equation 2.18 is the solution to Lighthill's equation (Eq. 2.8) with the presence of stationary solid boundaries and it is named Curle's Theorem. It should be noted that in Curle's original publication [23], the derivation of Equation 2.18 followed a different path. The derivation here follows the same approach proposed by Ffowcs Williams and Hawkings [24]. Next, the

same approach will be used to derive the equation and solution of Lighthill's equation with the presence of moving boundaries.

2.1.4 FW-H Equation

In the last subsection, Lighthill's theory is extended to account for a stationary boundary. Moreover, if the surface $f = 0$ is not stationary, i.e., $\frac{\partial H}{\partial t} \neq 0$, the momentum equation and continuity equation become

$$\begin{aligned} \frac{\partial}{\partial t}(\rho u_i H) + \frac{\partial}{\partial x_i}[c_0^2(\rho - \rho_0)H] &= (\rho u_i) \frac{\partial H}{\partial t} - \frac{\partial(T_{ij}H)}{\partial x_j} \\ &\quad + [\rho u_i u_j + (p - p_0)\delta_{ij} - \tau_{ij}] \frac{\partial H}{\partial x_j}, \end{aligned} \quad (2.19)$$

$$\frac{\partial}{\partial t}((\rho - \rho_0)H) + \frac{\partial}{\partial x_i}(\rho u_i H) = (\rho - \rho_0) \frac{\partial H}{\partial t} + \rho u_i \frac{\partial H}{\partial x_i}. \quad (2.20)$$

Once again, by taking the time derivative of rearranged continuity equation and gradient of rearranged momentum equation and subtracting one from another, one can get the following inhomogeneous wave equation:

$$\begin{aligned} \left(\frac{\partial^2}{\partial t^2} - c_0^2 \frac{\partial^2}{\partial x_i \partial x_i} \right) [(\rho - \rho_0)H] &= \frac{\partial}{\partial t}(\rho u_i \frac{\partial H}{\partial x_i}) \\ &\quad - \frac{\partial}{\partial x_i}[(\rho u_i u_j + (p - p_0)\delta_{ij} - \tau_{ij}) \frac{\partial H}{\partial x_j}] + \frac{\partial^2}{\partial x_i \partial x_j}(T_{ij}H) \\ &\quad + \frac{\partial}{\partial t}[(\rho - \rho_0) \frac{\partial H}{\partial t}] - \frac{\partial}{\partial x_i}[(\rho u_i) \frac{\partial H}{\partial t}]. \end{aligned} \quad (2.21)$$

If it is assumed the moving surface $f = 0$ does not deform, a velocity vector \mathbf{U} denotes the motion of that surface. By further simplifying Equation 2.21, the moving surface is described by

$$f(\mathbf{y}, t) = f \left(\mathbf{y} - \int_{t_0}^t \mathbf{U} d\tau \right) = 0.$$

$\frac{\partial f}{\partial t}$ can be related to the gradient of f and \mathbf{U} :

$$\frac{\partial f}{\partial t} = -\nabla f \cdot \mathbf{U}.$$

Then $\frac{\partial H}{\partial t}$ on the right-hand side of Equation 2.21 can be expressed as

$$\frac{\partial H}{\partial t} = \frac{\partial H}{\partial f} \frac{\partial f}{\partial t} = \delta(f)(-\nabla f \cdot \mathbf{U}) = -\mathbf{U} \cdot \nabla H = U_i \frac{\partial H}{\partial x_i}. \quad (2.22)$$

Time derivative on source terms of Equation 2.21 can be eliminated by substituting Equation 2.22 into Equation 2.21. The resulting equation is

$$\begin{aligned} \left(\frac{1}{c_0^2} \frac{\partial^2}{\partial t^2} - \frac{\partial^2}{\partial x_i \partial x_i} \right) [c_0^2(\rho - \rho_0)H] &= \frac{\partial}{\partial t} \left[(\rho(u_i - U_i) + \rho_0 U_i) \frac{\partial H}{\partial x_i} \right] \\ &\quad - \frac{\partial}{\partial x_i} \left[(\rho u_i(u_j - U_j) + (p - p_0)\delta_{ij} - \tau_{ij}) \frac{\partial H}{\partial x_j} \right] \\ &\quad + \frac{\partial^2}{\partial x_i \partial x_j} (T_{ij}H). \end{aligned} \quad (2.23)$$

Equation 2.23 is called FW-H equation [24] and it is also an inhomogeneous wave equation. The three source terms on its right-hand side are of monopole, dipole, and quadrupole types, respectively. In principle, surface $f = 0$ can be arbitrary. However, if $f = 0$ indicates the boundaries of moving solid objects, from the no-slip boundary conditions, one may have $U_i = u_i$ on $f = 0$ and further simplify Equation 2.23:

$$\begin{aligned} \left(\frac{1}{c_0^2} \frac{\partial^2}{\partial t^2} - \frac{\partial^2}{\partial x_i \partial x_i} \right) [c_0^2(\rho - \rho_0)H] &= \frac{\partial}{\partial t} \left(\rho_0 U_i \frac{\partial H}{\partial x_i} \right) \\ &\quad - \frac{\partial}{\partial x_i} \left[((p - p_0)\delta_{ij} - \tau_{ij}) \frac{\partial H}{\partial x_j} \right] + \frac{\partial^2}{\partial x_i \partial x_j} (T_{ij}H). \end{aligned} \quad (2.24)$$

It should be emphasized that Equation 2.24 is not a correct equation until $f = 0$ is set as the physical boundaries of solid objects. Equation 2.17 can be applied to solve equation 2.24 using Green's function, just like what is done to Equation 2.15. The detailed process will be demonstrated in the next subsection.

2.1.5 Farassat's Formulation 1 and 1A

Equation 2.24 includes three source terms on the right-hand side, so its solution is supposed to consist of three corresponding components: monopole, dipole, and quadrupole. However, Farassat's formulations were developed for aerodynamic propellers, and the quadrupole

as a sound emitter is not as effective as monopole and dipole in such applications. Therefore, the quadrupole part is neglected in the solution to Equation 2.24. In addition, for aerodynamic fans, the magnitude of blade surface pressure is much greater than that of surface shear stress. So viscous shear stress τ_{ij} is also neglected.

By using Equation 2.17, the monopole part of solution can be obtained as

$$[c_0^2(\rho - \rho_0)H]_{\text{monopole}}(\mathbf{x}, t) = \int_{-\infty}^t \int_{V_\infty} G \frac{\partial}{\partial \tau} \left(\rho_0 U_i \frac{\partial H}{\partial y_i} \right) dV(\mathbf{y}) d\tau, \quad (2.25)$$

where G is the free-space Green's function defined as

$$G = \frac{\delta(\tau - t + r/c_0)}{4\pi r}, \quad r = |\mathbf{x} - \mathbf{y}| \quad \text{for } \tau > t$$

$$G = 0 \quad \text{for } \tau \leq t.$$

Then with identities

$$G \frac{\partial}{\partial \tau} \left(\rho_0 U_i \frac{\partial H}{\partial y_i} \right) = \frac{\partial}{\partial \tau} \left(G \rho_0 U_i \frac{\partial H}{\partial y_i} \right) - \rho_0 U_i \frac{\partial H}{\partial y_i} \frac{\partial G}{\partial \tau},$$

$$G|_{\tau=\pm\infty} = 0,$$

and

$$\frac{\partial G}{\partial \tau} = -\frac{\partial G}{\partial t},$$

the monopole component can be expressed as

$$[c_0^2(\rho - \rho_0)H]_{\text{monopole}}(\mathbf{x}, t) = \frac{\partial}{\partial t} \int_{-\infty}^t \int_{V_\infty} \rho_0 U_i \frac{\partial H}{\partial y_i} G dV(\mathbf{y}) d\tau. \quad (2.26)$$

In the derivation of Equation 2.26, Leibniz integral rule is used to take the time derivative out of integrals. Then by using identity Equation 2.11, the volume integral can be evaluated as a surface integral, and it yields

$$\begin{aligned}[c_0^2(\rho - \rho_0)H]_{\text{monopole}}(\mathbf{x}, t) &= \frac{\partial}{\partial t} \int_{-\infty}^t \int_{f=0} \rho_0 U_i n_i G dS(\mathbf{y}) d\tau \\ &= \frac{\partial}{\partial t} \int_{-\infty}^t \int_{f=0} \rho_0 U_i n_i \frac{\delta(\tau - t + r/c_0)}{4\pi r} dS(\mathbf{y}) d\tau.\end{aligned}\quad (2.27)$$

For an arbitrary function of source time $F(\tau)$, source time integral can be evaluated as

$$\int_{-\infty}^t F(\tau) \delta(\tau - t + r/c_0) d\tau = \int_{-\infty}^t \frac{F(\tau) \delta(\tau - t + r/c_0)}{1 + \frac{\partial r}{\partial t}/c_0} d(\tau - t + r/c_0) = \left(\frac{F}{1 - M_r} \right)_{\tau=t-r/c_0}, \quad (2.28)$$

where $M_r = -\frac{1}{c_0} \frac{\partial r}{\partial t}$, representing the mach number of a point \mathbf{y} going towards the observer located at \mathbf{x} . Using Equation 2.28, Equation 2.27 becomes

$$[c_0^2(\rho - \rho_0)H]_{\text{monopole}}(\mathbf{x}, t) = \frac{\partial}{\partial t} \int_{f=0} \left[\frac{\rho_0 U_i n_i}{4\pi r (1 - M_r)} \right]_{\tau=t-r/c_0} dS(\mathbf{y}). \quad (2.29)$$

Similarly, using $G|_{y=\infty} = 0$, the dipole part can be expressed as:

$$[c_0^2(\rho - \rho_0)H]_{\text{dipole}}(\mathbf{x}, t) = -\frac{\partial}{\partial x_i} \int_{f=0} \left[\frac{(p - p_0) \delta_{ij} n_j}{4\pi r (1 - M_r)} \right]_{\tau=t-r/c_0} dS(\mathbf{y}). \quad (2.30)$$

At far field, the radiation pattern is similar to the pattern of plane waves,i.e.,

$$\frac{\partial}{\partial x_i} \approx -\frac{\hat{r}_i}{c_0} \frac{\partial}{\partial t}$$

where $\hat{r}_i = \frac{y_i - x_i}{|y_i - x_i|}$. Then, a far field dipole part of solution is

$$[c_0^2(\rho - \rho_0)H]_{\text{dipole}}(\mathbf{x}, t) = \frac{\hat{r}_i}{c_0} \frac{\partial}{\partial t} \int_{f=0} \left[\frac{(p - p_0) \delta_{ij} n_j}{4\pi r (1 - M_r)} \right]_{\tau=t-r/c_0} dS(\mathbf{y}). \quad (2.31)$$

If the exact formula that includes near-field effects is pursued, one needs to have the exact relation between the time derivative and gradient of Green's function.

Using Equation 2.17, the dipole part of solution is

$$[c_0^2(\rho - \rho_0)H]_{\text{dipole}}(\mathbf{x}, t) = \int_{-\infty}^t \int_{V_\infty} (p - p_0) \delta_{ij} \frac{\partial H}{\partial y_j} \frac{\partial G}{\partial y_i} dV(\mathbf{y}) d\tau. \quad (2.32)$$

Green's function obeys identity

$$\frac{\partial G}{\partial y_i} = \frac{1}{c_0} \frac{\partial}{\partial t} (\hat{r}_i G) + \frac{\hat{r}_i G}{r}.$$

If this identity is substituted into the Equation 2.32, with Equation 2.11, expression for dipole component can be obtained as:

$$\begin{aligned} [c_0^2(\rho - \rho_0)H]_{\text{dipole}}(\mathbf{x}, t) &= \frac{1}{c_0} \frac{\partial}{\partial t} \int_{f=0} \left[\frac{(p - p_0)n_i \hat{r}_i}{4\pi r(1 - M_r)} \right]_{\tau=t-r/c_0} dS(\mathbf{y}) \\ &\quad + \int_{f=0} \left[\frac{(p - p_0)n_i \hat{r}_i}{4\pi r^2(1 - M_r)} \right]_{\tau=t-r/c_0} dS(\mathbf{y}). \end{aligned} \quad (2.33)$$

Combining Equations 2.29 and 2.33, Farassat's Formulation 1 is obtained:

$$\begin{aligned} [c_0^2(\rho - \rho_0)H](\mathbf{x}, t) &= \frac{\partial}{\partial t} \int_{f=0} \left[\frac{(\rho_0 c_0 U_i + (p - p_0) \hat{r}_i) n_i}{4\pi c_0 r (1 - M_r)} \right]_{\tau=t-r/c_0} dS(\mathbf{y}) \\ &\quad + \int_{f=0} \left[\frac{(p - p_0) n_i \hat{r}_i}{4\pi r^2 (1 - M_r)} \right]_{\tau=t-r/c_0} dS(\mathbf{y}). \end{aligned} \quad (2.34)$$

In the first term on the right-hand side of this equation, the observer time derivative needs to be evaluated. In practice, this derivative can only be evaluated numerically. Alternatively, it would be more ideal if the aerodynamic noise can be computed based on source time derivatives, because the motion of surface f or the aerodynamic loading on the surface are explicit functions of source time rather than functions of observer time. If the observer time derivatives can be transformed to the source time derivatives, the formulation would be easier to use, and this would be the next step of derivation.

In previous derivations, four space/time variables were used: observer spatial and temporal coordinate \mathbf{x} and t , source spatial and temporal coordinate \mathbf{y} and τ . These variables are associated with each other through relation

$$\tau - t + \frac{|\mathbf{y} - \mathbf{x}|}{c_0} = 0. \quad (2.35)$$

For the sake of clarity, Lagrangian frame fixed with moving boundary $\boldsymbol{\eta}$ is introduced. In this frame, every material point on the moving boundary is designated with a specific value of $\boldsymbol{\eta}$. Then, naturally, in this frame any source point space coordinate \mathbf{y} is a function of its Lagrangian coordinate $\boldsymbol{\eta}$ and source time τ , that is, $\mathbf{y} = \mathbf{y}(\boldsymbol{\eta}, \tau)$. Then, take observer time derivative of Equation 2.35 to get: $\left(\frac{\partial \tau}{\partial t}\right)|_{(\mathbf{x}, \boldsymbol{\eta})} - 1 - M_r \left(\frac{\partial \tau}{\partial t}\right)|_{(\mathbf{x}, \boldsymbol{\eta})} = 0$. The former equation can be rearranged to yield the following identity that describes the relation between the speed of source motion and source/observer time

$$\left(\frac{\partial \tau}{\partial t}\right)|_{(\mathbf{x}, \boldsymbol{\eta})} = \frac{1}{1 - M_r}. \quad (2.36)$$

Equation 2.36 is an important identity that relates observer time t with source time τ . With this identity, chain rule can be utilized to evaluate observer time derivatives. For example, for observer time derivative of function $\phi(\mathbf{x}, \tau, \boldsymbol{\eta})$ can be evaluated as

$$\frac{\partial}{\partial t}[\phi(\mathbf{x}, \tau, \boldsymbol{\eta})]_{\tau=t-r/c_0} = \left[\frac{1}{1 - M_r} \frac{\partial \phi}{\partial \tau} \right]_{\tau=t-r/c_0}. \quad (2.37)$$

In Formulation 1 (Eq. 2.34), function ϕ could be U_i , n_i , \hat{r}_i , M_r , etc. The next step is evaluation of source time derivative of these variables. Here are some identities involved in the evaluation of $\frac{\partial \phi}{\partial \tau}$:

$$\begin{aligned} \frac{\partial r}{\partial \tau} &= M_r c_0, \\ \frac{\partial \hat{r}_i}{\partial \tau} &= \frac{\hat{r}_i M_r c_0}{r} - \frac{U_i}{r}, \\ \frac{\partial M_r}{\partial \tau} &= \frac{1}{c_0} \frac{\partial}{\partial \tau}(U_i \hat{r}_i) = \frac{\hat{r}_i}{c_0} \frac{\partial U_i}{\partial \tau} + \frac{c_0^2 M_r^2 - U_i U_i}{c_0 r}. \end{aligned}$$

In Equation 2.37, taking $\phi(\mathbf{x}, \tau, \boldsymbol{\eta}) = \frac{\rho_0 U_n(\tau, \boldsymbol{\eta})}{4\pi r(\mathbf{x}, \tau, \boldsymbol{\eta})(1 - M_r(\mathbf{x}, \tau, \boldsymbol{\eta}))}$ for monopole and $\phi(\mathbf{x}, \tau, \boldsymbol{\eta}) = \frac{(p(\tau, \boldsymbol{\eta}) - p_0)n_i(\tau, \boldsymbol{\eta})\hat{r}_i(\mathbf{x}, \tau, \boldsymbol{\eta})}{4\pi c_0 r(\mathbf{x}, \tau, \boldsymbol{\eta})(1 - M_r(\mathbf{x}, \tau, \boldsymbol{\eta}))}$ for dipole, Formulation 1 (Eq. 2.34) can be transformed as:

$$\begin{aligned} [c_0^2(\rho - \rho_0)H]_{\text{monopole}}(\mathbf{x}, t) = \\ \int_{f=0} \left\{ \frac{\rho_0}{4\pi r(1 - M_r)^2} \left[\frac{\partial}{\partial \tau} (U_i n_i) + \frac{(U_i n_i)(\hat{r}_j \frac{\partial U_j}{\partial \tau})}{c_0(1 - M_r)} + \frac{(U_i n_i)(c_0^2 M_r - U_i U_i)}{c_0 r(1 - M_r)} \right] \right\}_{\tau=t-r/c_0} dS(\mathbf{y}) \end{aligned} \quad (2.38)$$

and

$$\begin{aligned} [c_0^2(\rho - \rho_0)H]_{\text{dipole}}(\mathbf{x}, t) = \int_{f=0} \left\{ \frac{1}{4\pi c_0 r(1 - M_r)^2} \right. \\ \left. \left[(\hat{r}_i n_i) \frac{\partial}{\partial \tau} (p - p_0) + \frac{(p - p_0)(U_i n_i)(\hat{r}_i \frac{\partial U_i}{\partial \tau})}{c_0(1 - M_r)} \right. \right. \\ \left. \left. + \frac{(p - p_0)[c_0(\hat{r}_i n_i) - U_i n_i]}{r} + \frac{(p - p_0)(\hat{r}_i n_i)(c_0^2 M_r - U_i U_i)}{c_0 r(1 - M_r)} \right] \right\}_{\tau=t-r/c_0} dS(\mathbf{y}). \end{aligned} \quad (2.39)$$

The resulting formulae (Equations 2.38 and 2.39) are called Formulation 1A.

Equation 2.38 and 2.39 are the forms of Farassat's Formulation 1A to be used for wind turbine infrasound prediction. Formulation 1A is in different forms in Farassat's text [27], and the forms shown here are the forms directly implemented in the wind turbine infrasound prediction program. These formulations are surface integrals evaluated at retarded time $\tau = t - r/c_0$. When the surface $f = 0$ is in motion relative to the observer (microphone), the shape of the integral surface is deformed so that the sound emitted from any part of the surface reaches the observer at the same time. The trick to find the exact shape of the integral surface at retarded time will be introduced in the next chapter.

In Equation 2.38 and 2.39, subscripts monopole and dipole are used to represent different component of aerodynamic noise. The monopole component is related to net volume flow through surface $f = 0$. If the surface is neither moving nor perforated, $U_i = 0$, and the monopole component (Eq. 2.38) is equal to zero. When the surface is moving and non-perforated, the monopole component is non-zero only if the surface displaces a volume of the surrounding fluid. When applying Equation 2.38 on wings/blades, the monopole component

is non-zero only if the wing/blade has non-zero thickness. Therefore, in Farassat's text [27], monopole component is called *thickness* component alternatively. Likewise, the dipole component is also called *loading* component alternatively, because it's related to loadings applied on the surface.

Terms *thickness* and *loading* noise are preferred in the following text because terms monopole and dipole are ambiguous. The ambiguity of the term monopole and dipole often leads to a misconception that Equation 2.38 and 2.39 are explicit evaluations of monopoles and dipoles distributed on a moving surface. Acoustic monopole and dipole are related to net volume flux and net force respectively. However, it's possible to have non-zero thickness and loading noise when there is no net volume flux and net force, so long as the surface is moving. The study subject of this thesis is such a case, where monopole and dipole noise are merely induced by motion, instead of net volume flux or net force.

2.2 Wind Turbine Noise

2.2.1 Noise Mechanism

Wind turbine noise refers to the noise associated with the operation of wind turbines, including two general noise mechanisms: flow-induced noise and mechanical noise. Mechanical noise of wind turbines stems mainly from structural vibration of gearbox, generator, and auxiliaries. Vibration transmits through structures, such as nacelle, tower, and blades, and induces noise radiation. Flow-induced noise is associated with interactions between air flow and turbine blades. For a typical 2 MW wind turbine, in general, the sound power level of flow-induced noise is greater than that of mechanical noise, whereas the mechanical noise features a spikier spectrum and potentially causes more annoyance than flow-induced noise [28].

There are two paths of mechanical noise transmission: airborne path and structure-borne path. Airborne noise directly radiates into the air. Structure-borne noise firstly transmits through other structural components, then radiates from surfaces into the ambient air. Pinder compared contributions of individual wind turbine components to the total sound power level of a wind turbine [28]. He concluded that the annoyance caused by wind turbines

is likely to be a result of mechanical noise, especially the structure-borne noise caused by the gearbox, because of its tonal feature due to transmission error of gears.

Nowadays, the mechanical noise of wind turbines has been effectively reduced by using various engineering techniques [29]. Flow-induced noise is now the dominant noise source of wind turbines. This situation is aggravated by the fact that mechanical noise does not increase as much as flow-induced noise, as wind turbine size gets larger and larger.

The flow-induced noise associated with wind turbines can be categorized into three types: (i) steady thickness and loading noise, (ii) noise induced by an atmospheric turbulent gust, and (iii) self-noise of turbine airfoil, as detailed below.

Steady thickness and loading noise

Steady thickness and loading noise are essentially a result of blades rotation. The rotating blades periodically disturb and exert forces on surrounding air. As a result, it contributes mostly to components of blade passing frequency and its harmonics. The word *steady* should be understood in a rotating frame fixed on turbine blades. This type of noise is the only noise generated when, viewing in a rotating frame fixed on turbine blades, the inflow is perfectly steady on any part of the blade.

This noise-inducing mechanism can be extended to include the noise induced by the non-uniform inflow velocity profile. Non-uniform velocity profiles can be the results of the wakes of wind turbine towers or velocity gradient with altitude. When the inflow velocity profile is non-uniform, the inflow is no longer perfectly steady when viewing from the rotating frame fixed on turbine blades. However, the unsteadiness caused by the non-uniform velocity profile is periodic, which ends up modulating steady thickness and loading noise at the frequency of rotation.

Noise induced by atmospheric turbulent gust

Wind turbines operate within a turbulent atmospheric boundary layer. Turbulent gusts interact with turbine blades and induce aerodynamic noise. The properties of atmospheric turbulence directly determine the characteristics of the consequent aerodynamic noise. An

important concept regarding turbulence is the *energy cascade*. Energy cascade depicts the phenomenon that the large eddies tend to break up into small eddies and thus transfer energy to small eddies. The small eddies then break up into yet smaller eddies. This energy transfer from larger eddies to smaller eddies continues until the eddies are so small that energy dissipation due to viscosity dominates the scenario. Every turbulent flow follows this energy cascade, and the smallest scale of turbulence eddies is the Kolmogorov scale, at which all the remaining turbulence kinetic energy dissipates. A typical energy (wavelength) spectrum of turbulence is shown in Figure 2.2.

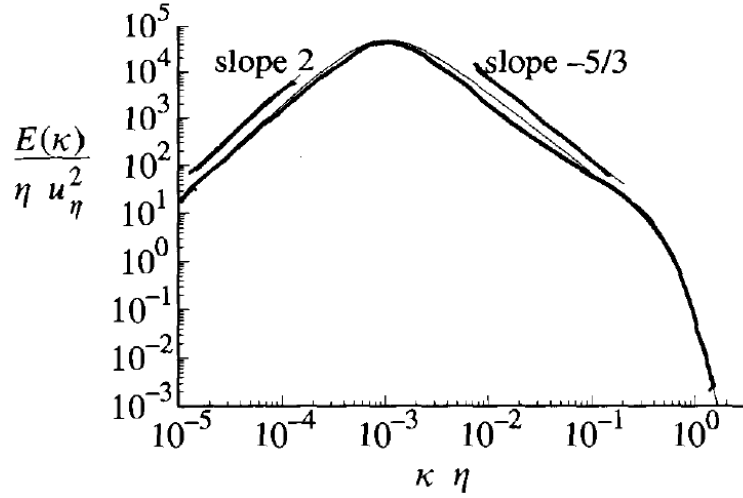


Figure 2.2. Typical Turbulence Energy Spectrum Normalized by Kolmogorov Scale η (From: Pope, 2000 [30])

Assume the chord length of blade is L_c , the characteristic wavelength of turbulence eddies is Λ and the eddies convect at velocity U , then, according to Taylor's frozen hypothesis [30], the characteristic frequency is:

$$f = \frac{U}{\Lambda}. \quad (2.40)$$

The wavelength of corresponding noise is:

$$\lambda_a = \frac{c}{f}. \quad (2.41)$$

If the dimension of the eddy is much larger than blade chord length: $\Lambda \gg L_c$, and assume the turbine blade motion is subsonic, combining 2.40 and 2.41, it yields $\lambda_a = \frac{c}{f} = \frac{c\Lambda}{U} = \frac{\Lambda}{M} > \Lambda \gg L_c$, which means the turbine blade sections can be regarded as acoustically compact noise sources. Specifically, each blade section can be regarded as a point dipole that can be determined by the unsteady force induced by a turbulent gust. Given the wavelength spectrum of turbulence, the force induced by turbulence, or namely a Fourier component of the wavelength spectrum, can be readily solved by using the Kemp-Sears method [31], which has been widely used in turbomachinery noise analysis.

If the dimension of the eddy is close to or smaller than blade chord length, wind turbine blade sections are no longer acoustically compact. The small eddies distort and shatter when they interact with the blade surface, and thus induce local load variation on the blade surface. Modeling of vortex-blade interaction leads to the study of vortex sound. Similar to what has been done by Lighthill, Howe took total fluid enthalpy as an independent variable and rearranged equations of fluid motion to yield his vortex sound equation [32]. The vortex sound equation is a convective wave equation, which reduces to wave equation without the presence of mean flow. The flow vorticity is explicitly included in the source term of the vortex sound equation so that the sound induced by vertices can be evaluated by solving the vortex sound equation.

Self-noise of turbine airfoil

Self-noise is the noise generated due to the instability of the blade boundary layer and its interaction with the blade surface. Self-noise occurs even if the inflow is perfectly uniform and steady. Possible reasons for wind turbine self-noise include trailing edge noise, vortex shedding, flow separation, surface imperfection, etc.

The trailing edge noise is a result of the interaction between the trailing edge and eddies in a boundary layer. What makes it different from the interaction between inflow turbulence and airfoil is the fact that the blade boundary layer gradually develops along the blade chord. Ffowcs Williams and Hall theoretically showed that the sharp trailing edge amplifies noise radiation induced by turbulent eddies in a boundary layer, and the amplification is affected

by the shape of the trailing edge [33]. Howe also investigated trailing edge noise by solving vortex sound equation [32]. His theory can not only be used in the analysis of a sharp trailing edge but also a blunt trailing edge. Amiet, on the other hand, coined the concept of the airfoil response function, which is derived from the solution of a linear PDE [34]. The airfoil response function can relate airfoil surface pressure change to turbulence eddies. Therefore, once the airfoil response function is solved, the wavenumber component of turbulence can be directed related to a convecting dipole on the blade surface. The trailing edge is considered to be the dominant high-frequency broadband noise of wind turbines.

Because of the apparent bluntness of wind turbine blades, vortex shedding can occur during wind turbine operation and result in a von Karman vortex street. The shedding is likely to occur at the trailing edge of a blade, yet the characteristic of noise induced by vortex shedding is different from that of trailing edge noise. Vortex shedding induces a tone at vortex street frequency.

Flow separation can occur on wind turbines when wind direction suddenly changes. Paterson *et al.* investigated the relation between noise source location and separation extent [35].

2.2.2 Prediction Methods for Wind Turbine Noise

There are mainly three categories of wind turbine noise prediction methods: analytical method, empirical model, and numerical simulation.

The analytical method includes the theories introduced in section 2.1. The computational approach used in this thesis is an implementation of an analytical method based on FW-H acoustics analogy theory. In particular, Farassat's Formulation 1A [27] is used. Farassat *et al.* have developed other time-domain formulations for different applications throughout the 1980s-1990s. The initial formulation in this category, Formulation 1, was published in 1975 [36]. Formulation 1A is directly derived from Formulation 1 by converting derivatives from observer frame to source frame [25]. Later, Formulation Q1 and Q1A were developed to predict quadruple noise components [37]. Formulation 1B was a further simplification of Formulation 1A and had been used in statistical analysis of broadband rotor noise because of its simplicity [38]. Formulation 3 was developed for supersonic rotor noise [39].

Based on extensive measurement of airfoil NACA 0012, Brooks *et al.* proposed a semi-empirical model for airfoil self-noise prediction [40], which is named after initials of researches as BPM model. In the BPM model, the sound pressure level prediction is based on a universal spectrum shape function that depends only on Strouhal number, with corrections related to Mach number, blade span, boundary layer thickness, and empirical scaling factor. Even though the BPM model is developed from measurement data of NACA 0012 airfoil, it has also been successfully applied on wind turbine noise prediction [41], even though NACA 0012 is very different from wind turbine airfoils.

Numerical simulation approaches of aerodynamics noise can be classified into two types: direct simulation and hybrid simulation. In a direct simulation, the sound is directly computed by solving non-linear equations of fluid dynamics. The computation resource required by direct simulation is so tremendous that the application of direct simulation is limited to cases with simple geometry and relatively low Reynolds number, such as airfoil [42] and cavity [43].

Hybrid simulation is the approach taken in this thesis. The use of hybrid simulation has been widely used in the noise prediction of rotors. In a hybrid simulation, the background flow field is simulated or modeled, and consequent aerodynamic noise is computed by solving either an ad hoc wave equation or a set of linearized PDE's [44].

3. METHODOLOGY

The major motive of this thesis is to develop a wind turbine aerodynamic noise prediction tool. In previous chapters, the working principles of wind turbines and fundamentals of aerodynamic noise have been reviewed. In this chapter, the working principle of wind turbines and aerodynamic noise theories are combined to establish a new method, Time Domain Rotor Infrasound Prediction (TDRIP), to characterize the infrasound emissions of wind turbines. The established methods are then programmed and validated so that the program be used as the wind turbine infrasound emission prediction tool.

The basic procedure of study is shown in Figure 3.1. Firstly, the blade airfoil is selected. Based on the selected airfoil, the performance of the airfoil is analyzed and the optimal angle of attack can be found from the airfoil analysis. With the optimal angle of attack, the shape of a wind turbine blade, particularly the installation angle and chord length, can be determined. The blade load distribution can also be determined in airfoil analysis. Then the shape of the blade and blade load are found are put into the aerodynamic noise prediction program. The program solves the FW-H equation (Eq. 2.23) to predict infrasound emitted from wind turbines.

3.1 Assumptions

Several key assumptions are adopted to simplify the analysis of this subject.

First of all, it is assumed that wind turbines are operated at the conditions of Betz's model, which means the flow field is steady and incompressible, and irrotational. With this assumption, the power coefficient of the wind turbine reaches max possible value. More importantly, in Betz's model, the axial induction factor is $a = 1/3$, and Equation 1.16 can be used to determine the shape of wind turbine blades.

Secondly, the tower of the wind turbine is neglected, and the wind turbine blades are assumed to be rotating at a steady speed and the rotor is perfectly rigid. This assumption simplifies the motion of the rotor. It means every material point on the rotor moves steadily on a circular trajectory, and it allows us to locate a certain part of the wind turbine at any

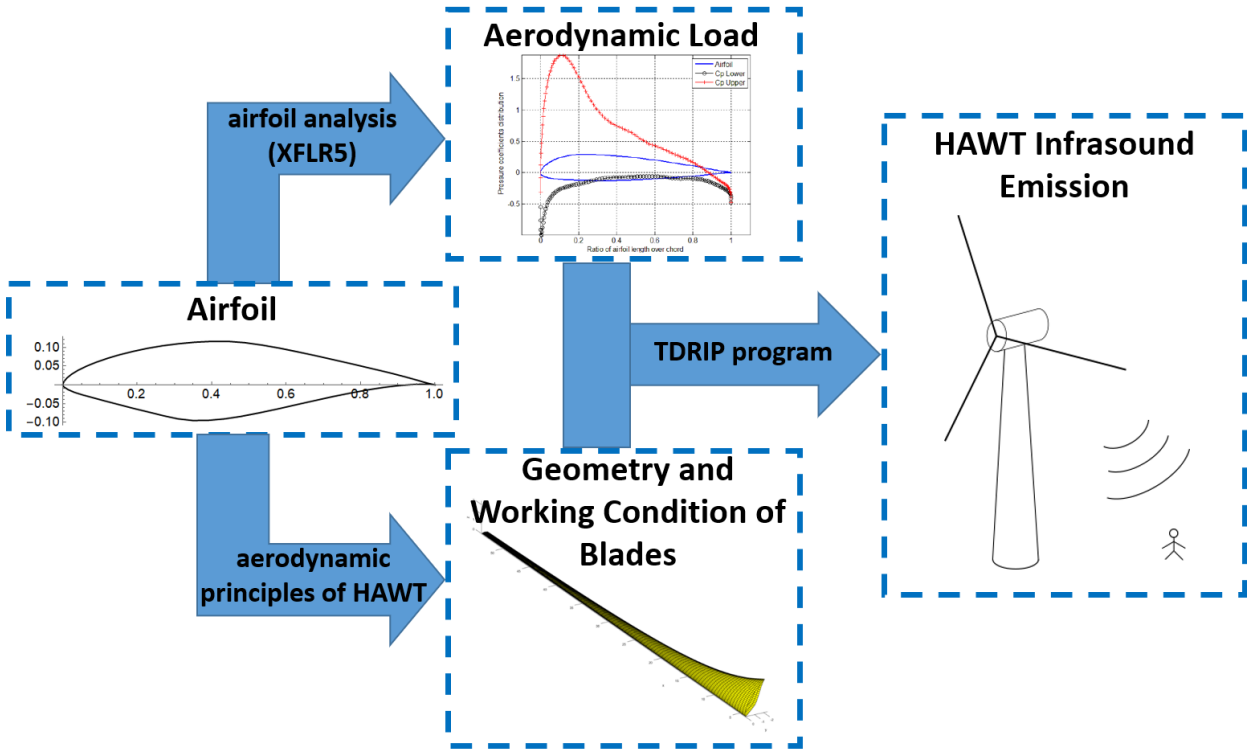


Figure 3.1. Methodology

time conveniently. With this assumption, the sound received by an observer can be easily traced back to a source in motion. The exact process will be introduced in section 3.2.

Additionally, the wind speed is assumed to have a uniform profile. In reality, wind speed may have a gradient (shear) varying with altitude, and the profile of wind speed also displays diurnal variation. As a result, the angle of attack at a certain section of the blade depends on its altitude and it would make the estimate of blade surface pressure much more complicated. This effect is neglected in the present study but will be considered in future studies.

Furthermore, when doing the tracing back from the microphone to the sound source, the effect of wind speed is neglected. Because sound is pressure disturbance traveling in fluid at speed of sound, when wind exists, sound wave emitted at certain location reaches a downwind microphone earlier than it reaching an upwind microphone. Taking wind speed into analysis thus significantly complicates the tracing back process. The normal horizontal axis wind turbine operates at a wind speed around approximately 10 m/s and the turbine would be locked if wind speed gets much higher to avoid damage to the wind turbine. This

nominal wind speed is approximately 3% of the speed of sound, which only results in 6% difference in emission time estimation at most. Thus it is reasonably neglected.

When analyzing wind turbines sitting on the ground, the ground surface is assumed to be a perfectly flat and locally reactive boundary. In the thesis, being locally reactive simply means the reflection coefficient of the ground is independent of the incidence angle of sound. There has been evidence that indicates most outdoor ground surfaces are locally reactive [45].

According to Lighthill's theory, the intensity of the quadrupole component obeys the eighth power law, which means its intensity is significant when the flow velocity is high. Thus, the analysis of aerodynamic sound emitted from wind turbines, the quadrupole noise component, which is generated from turbulence gusts, is neglected. As for the dipole (loading) component, only the noise induced by *locally steady* load is considered. The locally steady load is the component of the blade surface that does not change over time if measured in a frame rotating with the rotor. In other words, if a pressure transducer is fixed on a turbine blade, the reading of *locally steady* load does not change over time. The unsteady mechanisms, such as turbulence boundary layer or flow separation, are not taken into account in the TDRIP. This suggests surely a sacrifice of accuracy, to a certain extent, in exchange for efficiency. Yet in section 4.1, by referring to high-fidelity CFD results, an attempt is made to justify that the locally steady mechanism is more significant than the locally unsteady mechanism in terms of infrasound emission and possible environmental issues caused by wind turbines.

3.2 Shape and Pressure Distribution of Wind Turbine Blade

In the present work, an NREL wind blade airfoil, S816 (Figure 3.2), is selected to construct the entire blade. S816 airfoil is a thick airfoil designed for horizontal axis wind turbines by Somers [46]. S816 displays optimal performance at the middle span region of a wind turbine blade. Airfoils of the same family have been adopted and tested on an NREL's experimental wind turbine [47].

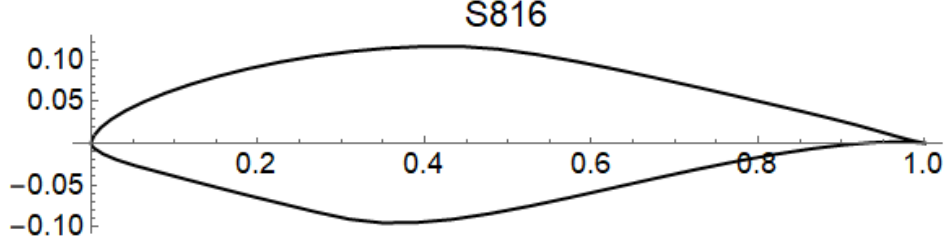


Figure 3.2. NREL’s S816 Airfoil at $\alpha = 0^\circ$

The performance of the S816 airfoil, i.e., its lift-drag characteristics, is analyzed using XFLR5 software [48]. The maximum lift-drag ratio of the airfoil is reached at $\alpha = 4^\circ$, where $L/D = 159.7$. Pressure coefficient distribution at this condition is shown in Figure 3.3b.

The twist and chord length distribution along blade span is computed based on Equation 1.16. The dimensions of the wind turbine are in Table 3.1. Distributions of relative wind angle φ and chord length L_c with respect to relative span location r/R are shown in Figure 3.5. The resulting blade is shown in Figure 3.6. As shown in Figure 3.6, a blade consists of 100 sections from root to tip, and each section consists of 65 quadrilateral elements. In total, the model used in TDRIP consists of 19500 quadrilateral elements.

Table 3.1. Wind Turbine Dimensions

Number of Blades B	3
Blade Length	50 m
Hub Diameter	8 m
Rotor Diameter D_{rotor}	108 m
Hub Height H_{hub}	120 m
Rotational Speed Ω	10 rpm
Wind Speed	12 m/s
TSR λ	4.71

3.3 Principle of TDRIP

The core of TDRIP is a rotor noise prediction program. The program is developed in MATLAB and it is essentially an implementation of Farassat’s Formulation 1A (Equations 2.38 and 2.39) introduced in Section 2.1. Farassat’s Formulation 1A is essentially a surface integral. The surface of the wind turbine rotor is chosen to be the integral surface because

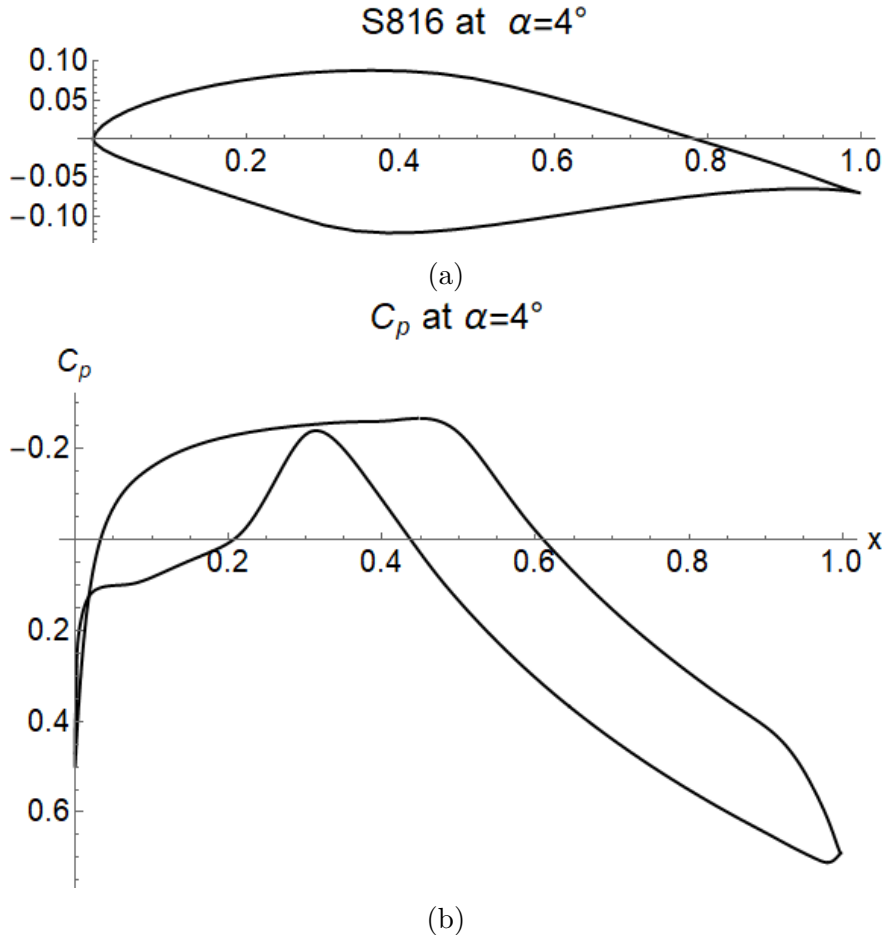


Figure 3.3. (a) S816 airfoil at $\alpha = 4^\circ$ and (b) pressure coefficient distribution at $\alpha = 4^\circ$

the shape and load distribution of the wind turbine rotor can be determined using methods in Section 3.2. In the TDRIP program, the wind turbine rotor is discretized into surface elements and the contribution of each element is evaluated. Some technical details of TDRIP program will be shown and discussed in the following subsections.

3.3.1 Element and Observer

The TDRIP program is object-oriented and two major classes are defined: Element and Observer. Each individual element object represents a quadrilateral element shown in Figure 3.6 and contains properties related to geometry, motion, and force of an element. An observer object includes properties and methods related to ground effect and aerodynamic noise computation.

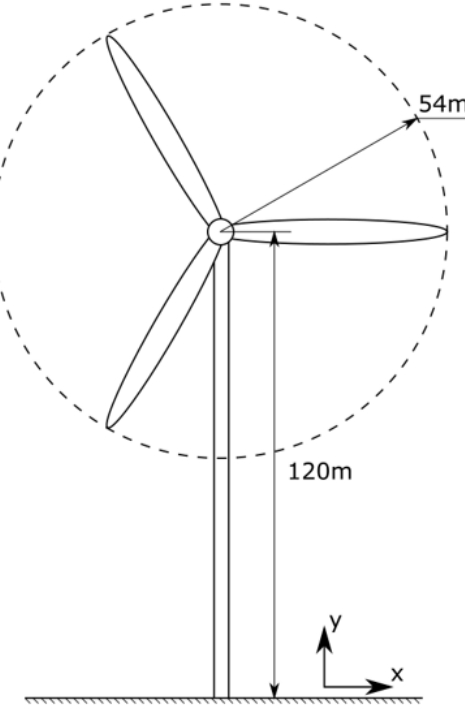


Figure 3.4. Wind Turbine Schematic

A static method that computes the location of an element at a certain source time is defined in the Element class. Because it has been assumed that the turbine blades are rotating at a steady speed, the distance between an element and an observer $r(\tau)$ is

$$r(\tau) = \left\| \begin{bmatrix} \cos(\Omega\tau) & -\sin(\Omega\tau) & 0 \\ \sin(\Omega\tau) & \cos(\Omega\tau) & 0 \\ 0 & 0 & 1 \end{bmatrix} \left(\mathbf{r}_0 - \begin{bmatrix} 0 \\ H_{hub} \\ 0 \end{bmatrix} \right) + \begin{bmatrix} 0 \\ H_{hub} \\ 0 \end{bmatrix} - \mathbf{r}_{observer} \right\|, \quad (3.1)$$

where Ω is rotor angular velocity, \mathbf{r}_0 is the initial location of an element, $\mathbf{r}_{observer}$ is the location of the observer. Equation 3.1, combined with Equation 2.35, source time t can be computed with given observer time τ .

Some details in the computation of retarded source time in observer class are worth extra attention and clarification. In the program, Equation 2.39 is evaluated at $\tau = t - r/c_0$ to get the sound pressure at t at a certain observer. For the convenience of signal processing, sound pressure is uniformly sampled on observer time t . However, because the trajectory of each element is not a straight line, uniform samples of observer time t do not correspond to

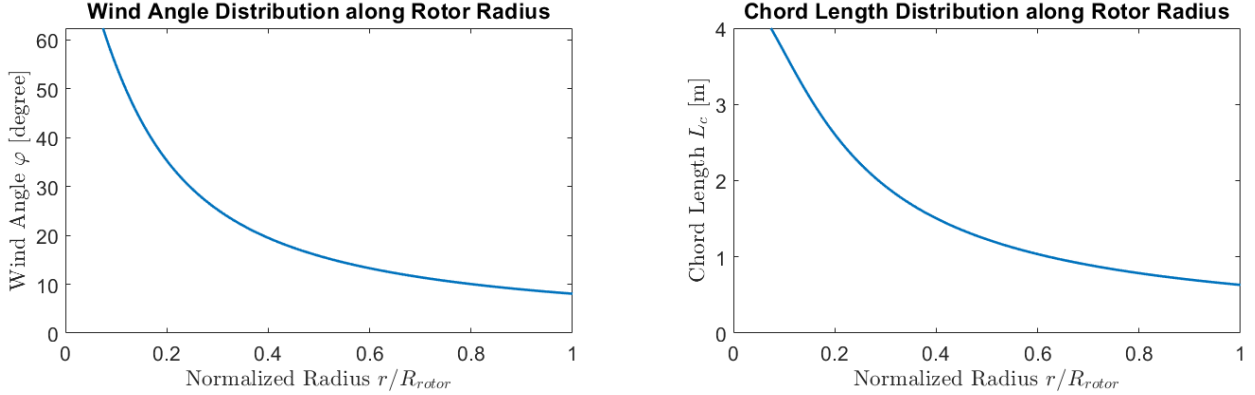


Figure 3.5. Twist and chord length distributions

uniform samples of source time τ . In other words, the sound emitted from different elements at a certain time does not reach the observer at the same time. As a result, τ needs to be evaluated on every single element for every observer time step. Figure 3.7 shows an example of the relation between t and τ for a certain element-observer pair. The element is taken from the tip of blade shown in Figure 3.6 and the observer is on the ground and $5D_{rotor}$ away from the turbine rotor ($R_{mic} = 0$, $\theta_{mic} = 0$ in Fig. 4.3b).

It should be noted that $r = r(\tau)$. Therefore $\tau = t - r/c_0$ is an implicit equation of $\tau(t)$, for which, in general, cannot be analytically solved. A generic approach is to find $\tau(t)$ for each element by using bisection method [27]. However, the use of the bisection method or other iterative numerical methods is too time-consuming for our application. Instead, the periodicity of element motion is utilized to develop a fast way to evaluate retarded time $\tau = t - r/c_0$.

Because the evaluation of observer time $t = \tau + r/c_0$ is explicit if source time τ is known, interpolation function $t = t(\tau)$ can be created from a series of (τ_i, t_i) pairs. Then $\tau = \tau(t)$ can be found by simply taking the inverse of the interpolation function. Once $\tau = \tau(t)$ has been found, τ_j can be evaluated when corresponding observer time t_j are given as a set of uniformly spaced time steps. The existence of inverse function is guaranteed, so long as the motion of element is not supersonic [27]. The existence of inverse function can also be confirmed by looking at the graph of $t(\tau)$ (e.g. inverse of Fig. 3.7). The fact that function $\tau(t)$ is a monotonic increasing function guarantees the existence of inverse function $t = t(\tau)$.

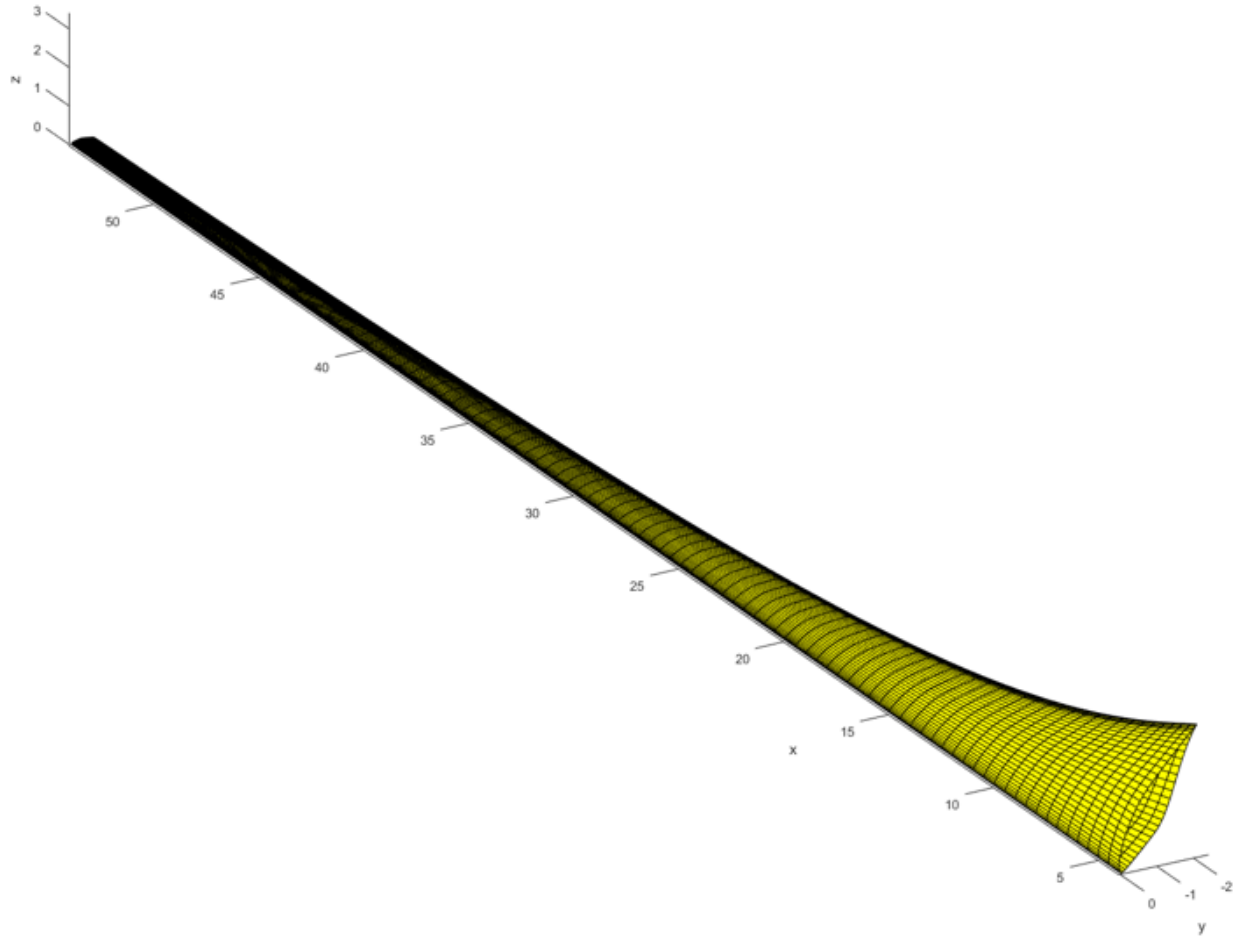


Figure 3.6. Wind Turbine Blade in TDRIP

When the source doesn't move, $\tau(t)$ would be a straight line of which slope is 1. When the source is moving towards the observer, the slope of $\tau(t)$ gets greater than 1 and vice versa. Moreover, when the element moves at the speed of sound, the curve of $\tau(t)$ would be either horizontal or vertical, depending on the direction of motion. When $\tau(t)$ is vertical, the sound emitted at different source time t is received by the observer at the same observer time τ , and that indicates a normal shock wave. When the element moves in supersonic speed, $\tau(t)$ is no longer monotonic increasing, which means the sound received at a certain observer time can possibly be emitted on different source times, and the existence of inverse function $t = t(\tau)$ is denied. Figure 3.7 visualizes Equation 2.36 that relates source time and observer time and shows how $\tau(t)$ evolves as M_r increases.

If the source element is in a motion with period T_0 , observer time obeys the following relation:

$$\tau(t + T_0) = \tau(t) + T_0. \quad (3.2)$$

This relation means the observer time is delayed by T_0 if the source time is delayed by T_0 .

An alternative form of Equation 3.2 is

$$\tau(t) = \tau(t - kT_0) + kT_0. \quad (3.3)$$

In Equation 3.3, letting k be the quotient of t/T_0 , then $t - kT_0$ is always between 0 and T_0 , that is, $0 \leq t - kT_0 < T_0$. This inequality means only on $t \in [0, T_0)$ should $\tau(t)$ be evaluated. When t is greater than T_0 , the value of $\tau(t)$ is equal to $\tau(t - kT_0) + kT_0$, in which $\tau(t - kT_0)$ is within the range $[0, T_0)$.

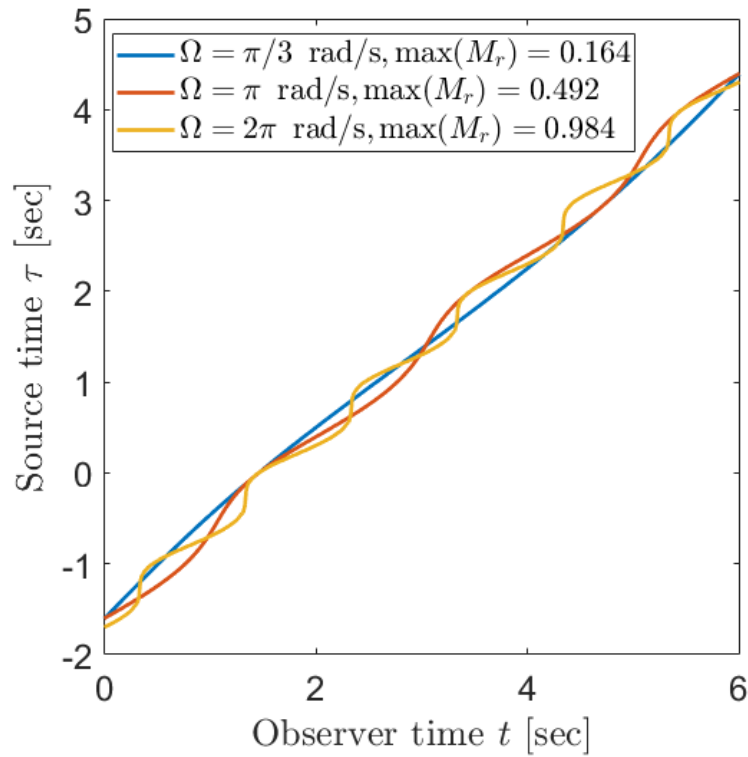


Figure 3.7. Observer Time t vs. Source Time τ

Equation 3.3 essentially renders a efficient way to find corresponding retarded source time τ given observer receiving time t . In the program, each element-observer pair is associated

with a interpolation function $\tau = \tau(t)$ defined on $0 \leq t < T_0$. Compared with using iterative numerical method to solve for $\tau = \tau(t)$ at every single observer time step, evaluation of Equation 3.3 greatly increase the efficiency of computation.

3.3.2 Ground Effect

The ground effect has been considered in the computation of wind turbine infrasound emission at a location away from the turbine. The ground effect has been extensively investigated in the study of outdoor acoustics. A common treatment is to use a semi-empirical model to predict the frequency-dependent impedance of the ground surface.

The ground impedance formulation adopted in the program is a low frequency (<100 Hz) approximation of a model introduced by Attenborough [45]:

$$Z_c = 0.218(\sigma_e/f)^{1/2}(1+j), \quad (3.4)$$

where f is frequency, Z_c is ground surface normal impedance normalized with respect to air and σ_e is effective flow resistance. For sandy soil, $\sigma_e = 315000$ MKS.

Equation 3.4 is a frequency domain formulation. However, the formulation for sound computation (Equations 2.38 and 2.39) is in time domain. To adopt Equation 3.4 in the program, the impulse response of reflection coefficient $R(t)$ of ground surface is computed and it is convoluted with incident sound in time domain to compute reflected sound from ground surface. Reflection coefficient is:

$$\hat{R}(f) = \frac{1 - 1/Z_c}{1 + 1/Z_c}. \quad (3.5)$$

The problem of adopting reflection in the time domain is equivalent to finding the impulse of a digital filter with frequency response $\hat{R}(f)$. Its impulse response is

$$R(t) = \int_{-\infty}^{+\infty} \hat{R}(f) \exp(+j2\pi ft) df. \quad (3.6)$$

Figure 3.8 shows $\hat{R}(f)$ and $R(t)$. $\hat{R}(f)$ is shown up to sampling frequency $f_s = 32$ Hz. In practice, only the first half (up to 16 Hz) is computed by using the ground impedance model,

and the second half of $\hat{R}(f)$ is the complex conjugate of the first half, just to guarantee the impulse response will be real. Around $f_s/2$, $\hat{R}(f)$ is modified so that it goes to zero gracefully to avoid aliasing in IDFT. $R(t)$ is a 128 points impulse response with $-2 \leq t < 2$.

Figure 3.9 is an example of the incident and reflected sound with $\hat{R}(f)$ being the reflection coefficient. The thickness noise component emitted from one section of the blade (Fig.3.6) is computed. The emitted sound reaches the ground at a certain location and gets reflected. For this case, the reflected wave is very similar to the incident wave, because $\hat{R}(f)$ is very close to unity at the frequency of incident sound (0.5 Hz).

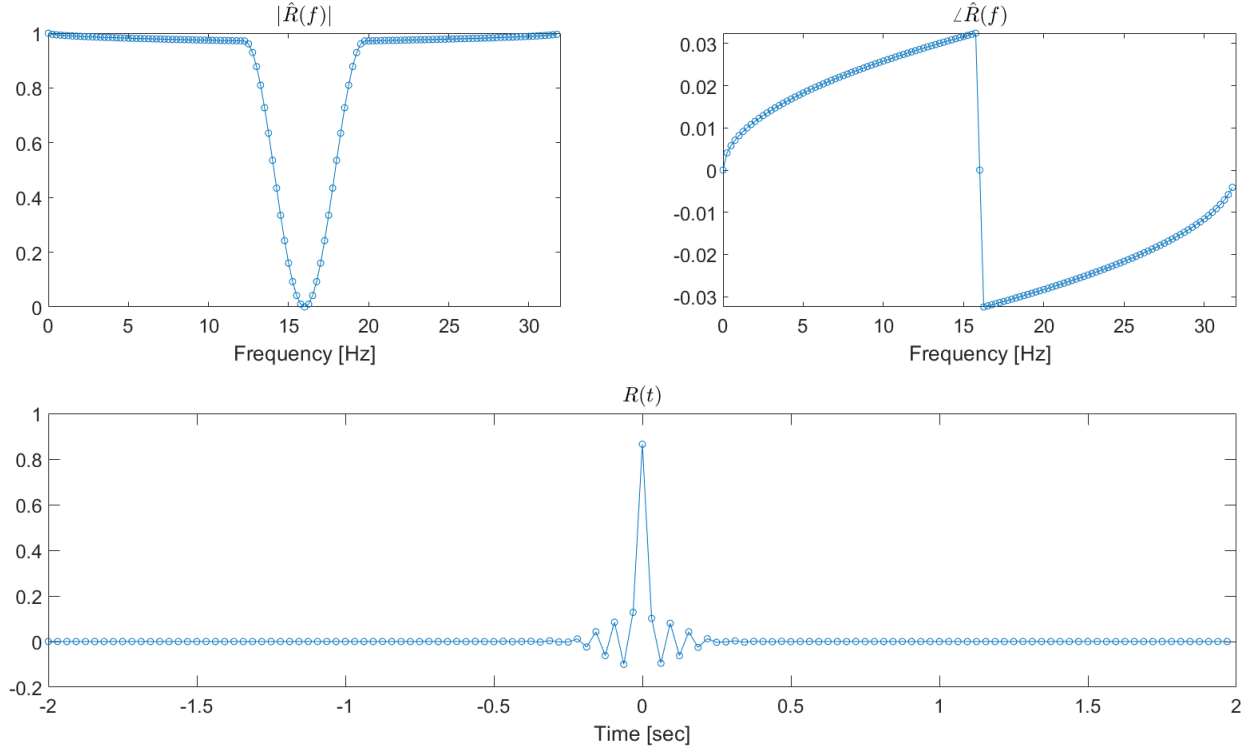


Figure 3.8. Reflection Coefficient and its Impulse Response

In time domain, the reflected sound pressure $p_r(t)$ is convolution of incident pressure $p_i(t)$ and $R(t)$

$$p_r(t) = p_i(t) * R(t) = \int_{-\infty}^{+\infty} p_i(\tau) R(t - \tau) d\tau. \quad (3.7)$$

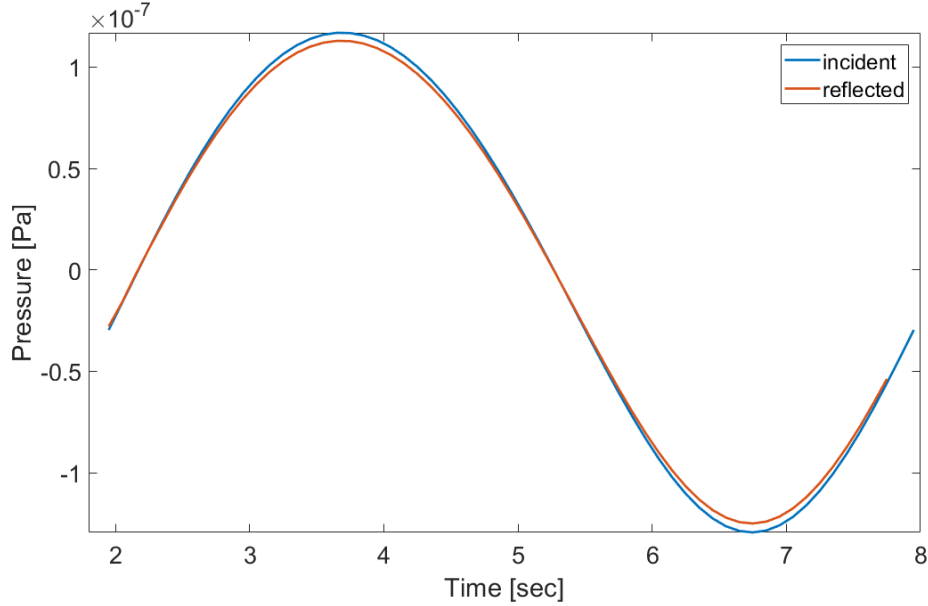


Figure 3.9. Incident wave and reflected wave on ground

Equation 3.7 implies that the time history of incident sound $p_i(t)$ is needed to compute the time history of reflected sound $p_r(t)$. Time history of $p_r(t)$ is 4 seconds shorter than that of $p_i(t)$.

The sound reaches the observer (microphone in Fig.3.10) at certain observer time is a combination of direct propagated sound $p_d(t)$ reflected sound $p_r(t)$. It should be noted that $p_i(t)$ and $p_r(t)$ are not emitted at the same time. To that end, the incidence point on the ground is regarded as secondary sound source, and the retarded time of ground source can be determined by evaluating (Fig. 3.10):

$$t - \tau_{\text{ground}} = \frac{h_{\text{mic}}(t - \tau_{\text{imag}})}{h_{\text{mic}} + h_{\text{source}}}, \quad (3.8)$$

where τ_{imag} is retarded time of the imaginary source that can be computed in the way described in subsection 3.3.1, h_{mic} and h_{source} are height of microphone and source from ground at τ_{imag} . The location of incidence is where the line joining microphone and imaginary source intersects ground. It should also be noted that the sound emitted from imaginary source is not used in the computation of sound at microphone. The purpose of imaginary source is just to determine τ_{imag} .

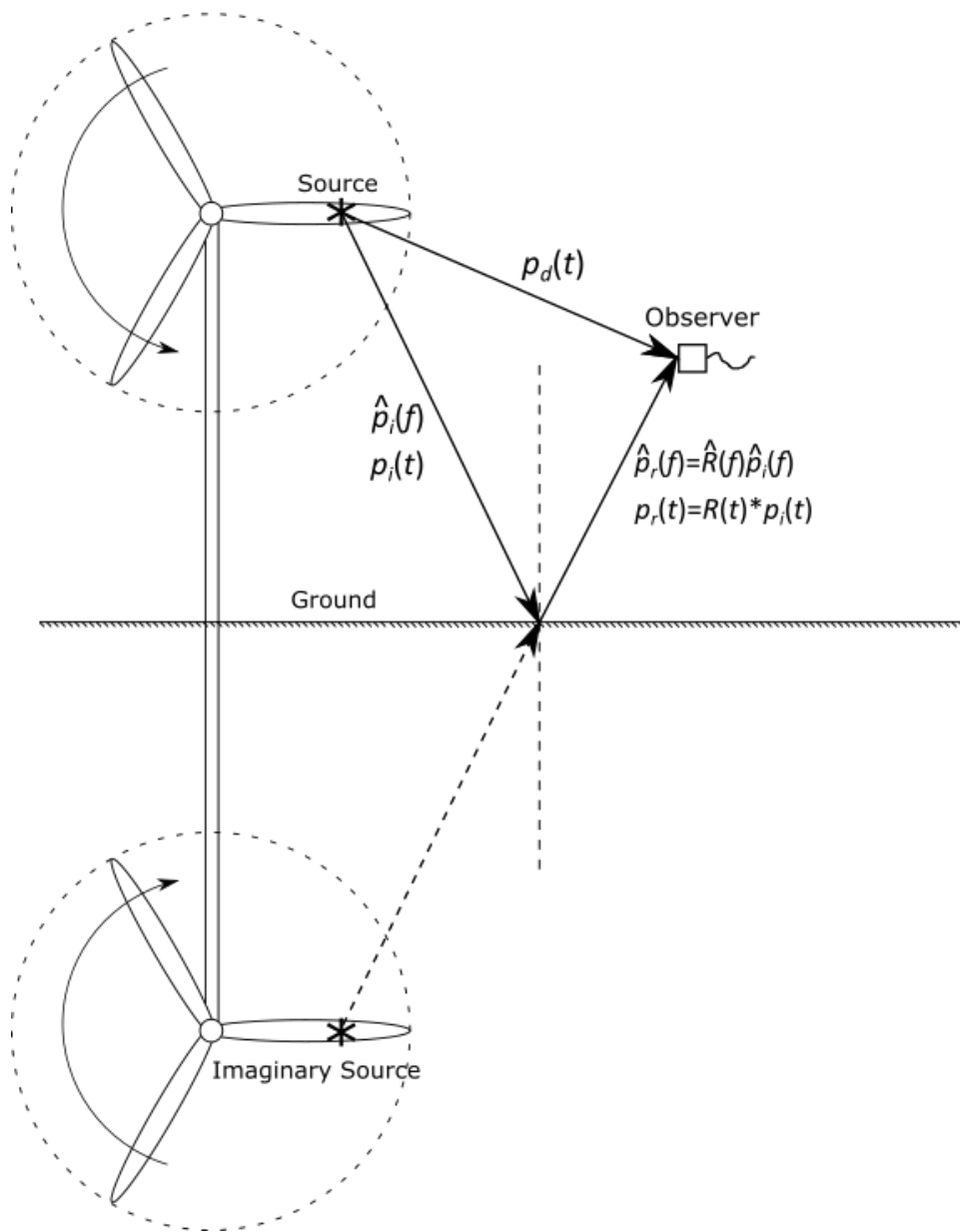


Figure 3.10. Reflection from Ground Surface

A side note about the ground effect is that the samples of incidence sound on the ground are not uniformly sampled if the reflected and direct sound are about to reach the microphone at the same time. That's because the location where reflection occurs changes with time. Specifically, the reflection point associated with a certain element moves in an oval path on the ground. In theory, the incident sound needs to be re-sampled to get a uniformly sampled signal to compute convolution. In practice, however, this issue is circumvented by restricting observers(microphones) on the ground, so that the $\tau_{\text{ground}} = t$ in Equation 3.8. This is an acceptable compromise for this study because the subject of study is of 120 m hub height, which is much higher than a human body or a normal house near a wind farm. However, it's necessary to resample incident sound if the TDRIP program is used to study wind turbine infrasound, or aerodynamic noise in general, perceived by skyscraper residents.

3.4 Validation of Program against CFD

A simple case is setup to validate the aerodynamic noise computation. Even though the program is developed for computing the aerodynamic noise of wind turbines, it is capable to compute the aerodynamic noise of any object in steady rotary motion. For the sake of simplicity, the aerodynamic noise of a rotating sphere is computed using the program and the results are compared with CFD results.

The computation domain of the case is shown in Figure 3.11. The dimension of the domain is $200\text{m} \times 200\text{m} \times 200\text{m}$. The CFD domain consists of 243k cells in total, with a stationary sub-domain(bounded by white edges in Fig. 3.11b) and rotating sub-domain(bounded by yellow edges in Fig. 3.11b). The Arbitrary Mesh Interface (AMI) technique of OpenFOAM is used to simulate the sliding boundaries between stationary and rotating sub-domains.

Table 3.2. Sphere

radius of sphere	2 m
radius of rotation	30 m
angular speed	$\pi/2$ rad/s
number of sphere surface element	320
Mach number	0.0687
Reynolds Number	6.22×10^6

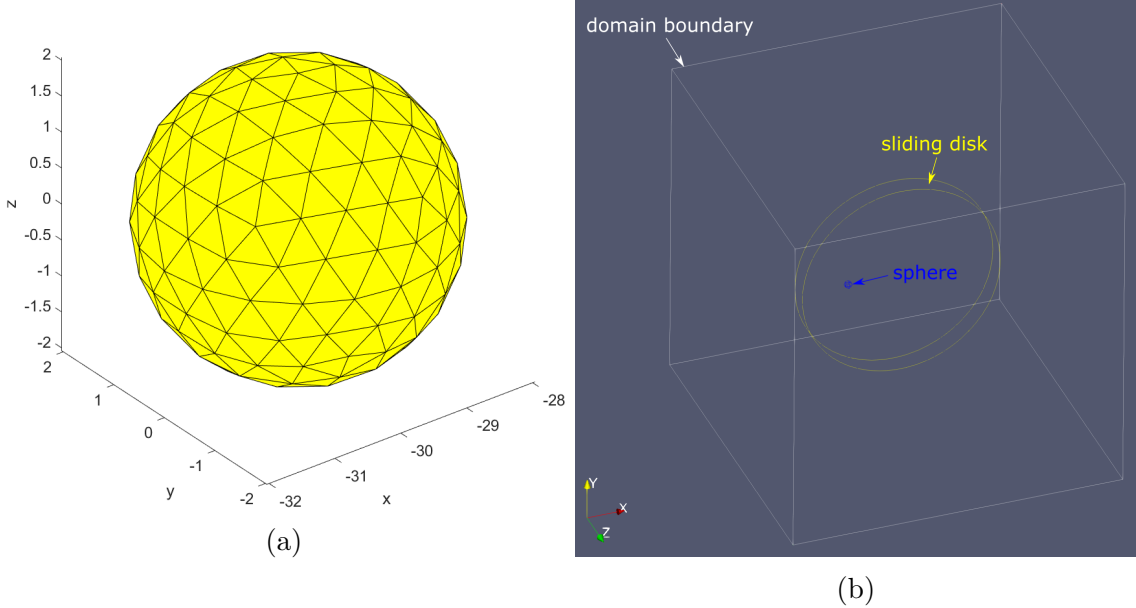


Figure 3.11. (a) sphere surface element and (b) CFD computation domain

In CFD, the aerodynamic sound is computed using a third-party open-source library *libAcoustics* [49] of OpenFOAM. The computation of *libAcoustics* is also based on Farassat's Formulation 1A, so that its results can be used for validation. Because the pressure coefficient distribution along the spherical surface is not available, only the thickness noise (Eq. 2.38) is computed using either the program or CFD. It should be noted that a few mistakes exist in the implementation of Formulation 1A of *libAcoustics*. The author of this thesis found and corrected the mistakes in the local copy of the source code, but the mistakes still exist in the newest release of *libAcoustics* [50] as of the day of the dissertation.

Aerodynamic noise is computed along the line of data points shown in Figure 3.12. The line is parallel to Z-axis, so the data points are denoted by their Z-coordinate. The sound pressure computed on a few data points is shown in Figure 3.13. OpenFOAM *libAcoustics* and the TDRIP program show good agreement on those data points. The period of 4 seconds ($\Omega = \pi/2$ rad/s) can be clearly identified in Figure 3.13. The waveform is highly distorted when the data point is in the plane of rotation (Z=0 m in Fig. 3.13). On the data points far away from the plane of rotation, however, the waveform is similar to a sinusoidal waveform (Z=200 m in Fig. 3.13). Doppler effect is the reason for waveform distortion. The thickness(monopole) noise is modulated by Doppler factor $1/(1 - M_r)$ as shown in Equation

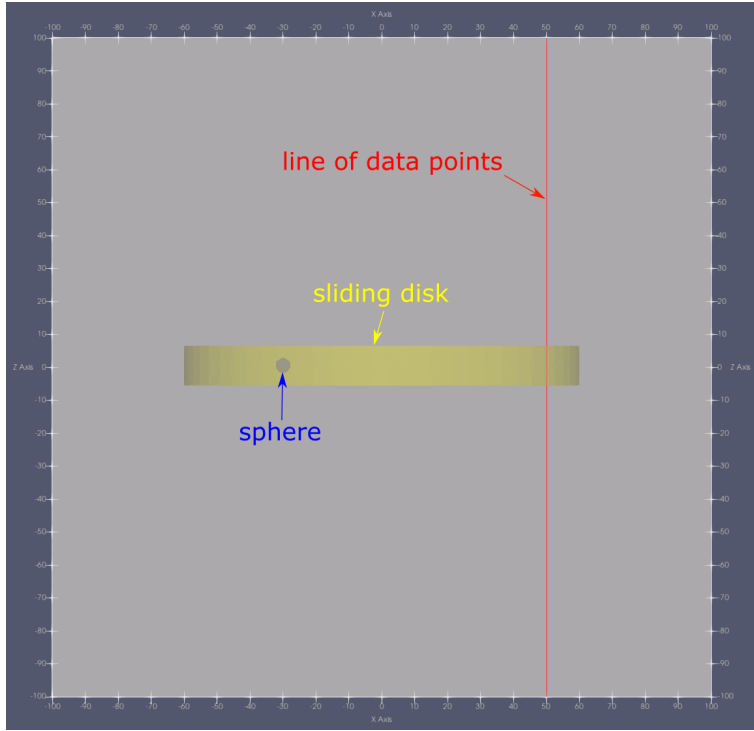


Figure 3.12. Line of Data Points

2.38. When observed from a data point on the plane of rotation, variation of Doppler factor is much greater than that observed from a data point far away from the plane of rotation. Additionally, when a data point is located on the axis of rotation, the Doppler factor has no variation. When $1/(1 - M_r)$ has no variation, Equation 2.29 leads to a conclusion that the thickness noise is zero along the axis of rotation. In fact, the variation in the Doppler factor determines the directivity pattern. The directivity pattern of one turbine will be shown in the next chapter. The counterintuitive 8-shape directivity for a single turbine, where the noise is maximized on the left and right sides and minimized on the front and back sides of the turbine, can be explained by this fact.

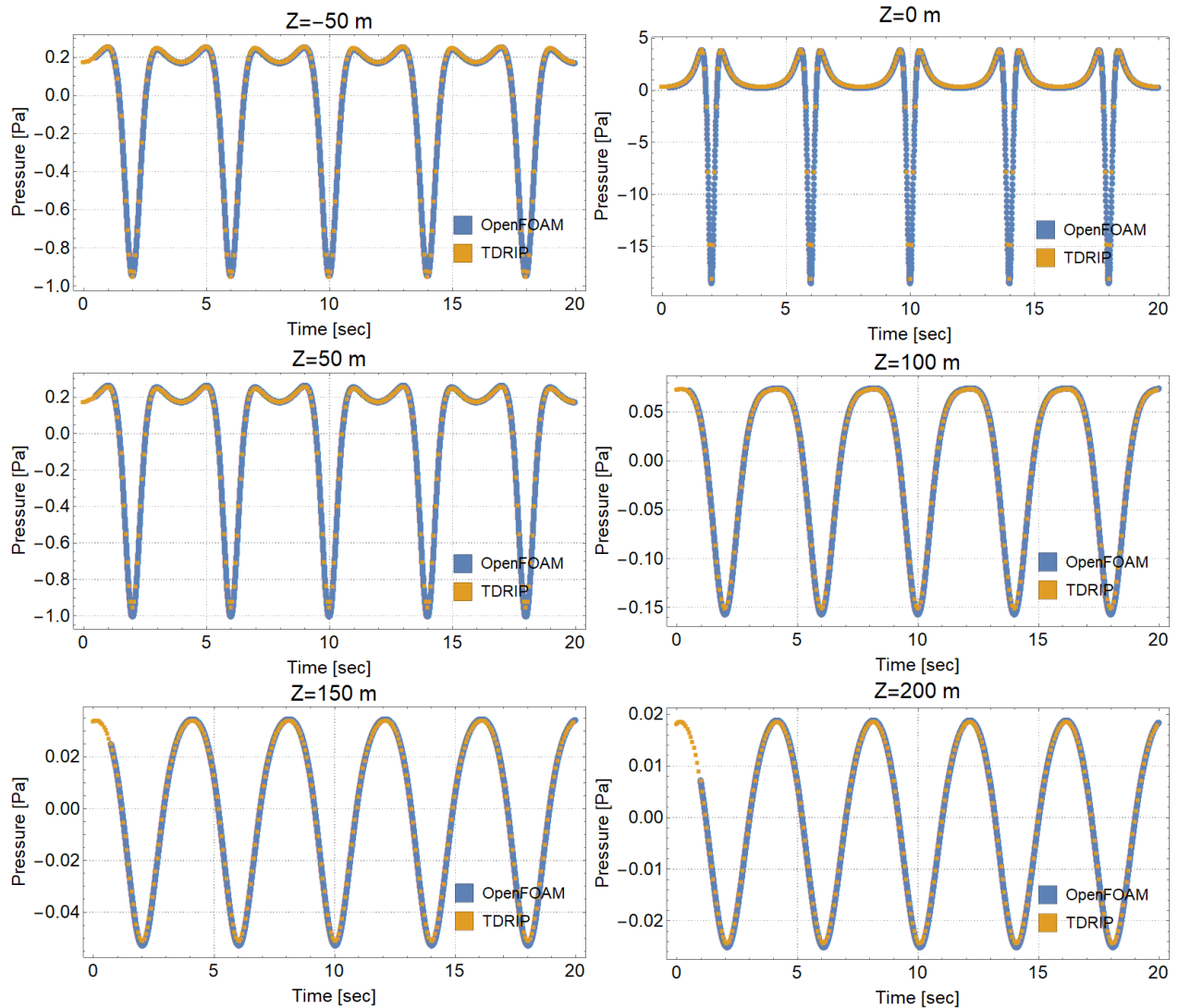


Figure 3.13. Thickness Noise Computed using OpenFOAM and TDRIP Program

4. RESULTS

In the previous chapter, we've established the methods to predict wind turbine aerodynamic noise and a program is developed using MATLAB for the prediction of wind turbine aerodynamic noise. In this chapter, the aerodynamic noise of the wind turbine is computed using the developed TDRIP program. Firstly, the aerodynamic noise of one turbine is computed using both TDRIP program and CFD. Then, the cases with two turbines are computed. The effect of wind turbine rotation phase difference and wind direction are demonstrated and discussed. By showing the data, the capabilities of the developed wind turbine aerodynamic noise prediction tool are demonstrated.

4.1 Infrasound Emitted from Single Turbine

In Chapter 3, we've compared the thickness noise computed by TDRIP program and CFD and the results are in good agreement. However, the CFD result and MABLAD result of loading noise are not directly comparable. The computation of loading noise is related to the surface load of wind turbine blades (Eq. 2.39), yet the TDRIP program only accounts for the locally steady part of the surface load. With known C_p distribution (Fig. 3.3b), the locally steady loading can be simply computed by using Equation 1.2. However, for a real operating wind turbine, there are many factors that contribute to locally unsteady surface load, such as turbulent boundary layer, atmospheric turbulent gust, flow separation, and instabilities, some of which are simulated or modeled in CFD computation.

The distinction of locally steady loading noise is its spectrum. The locally steady loading noise and thickness noise are narrowband noise at the BPF of a turbine, whereas the locally unsteady noise is broadband. The broadband CFD result is compared with the hearing threshold just to show the role of locally unsteady loading noise in the aerodynamic noise emission of a large wind turbine.

The CFD setup is shown in Figure 4.1. The structure of the computation domain is the same as that of the rotating sphere (Fig. 3.11b), with a rotating disk sub-domain containing the turbine rotor. The size of the domain is 540m×540m×540m, consisting of 3.57 million cells. Wind velocity is (0,0,12) m/s and the inlet of wind is located at Z=-101.5 m.

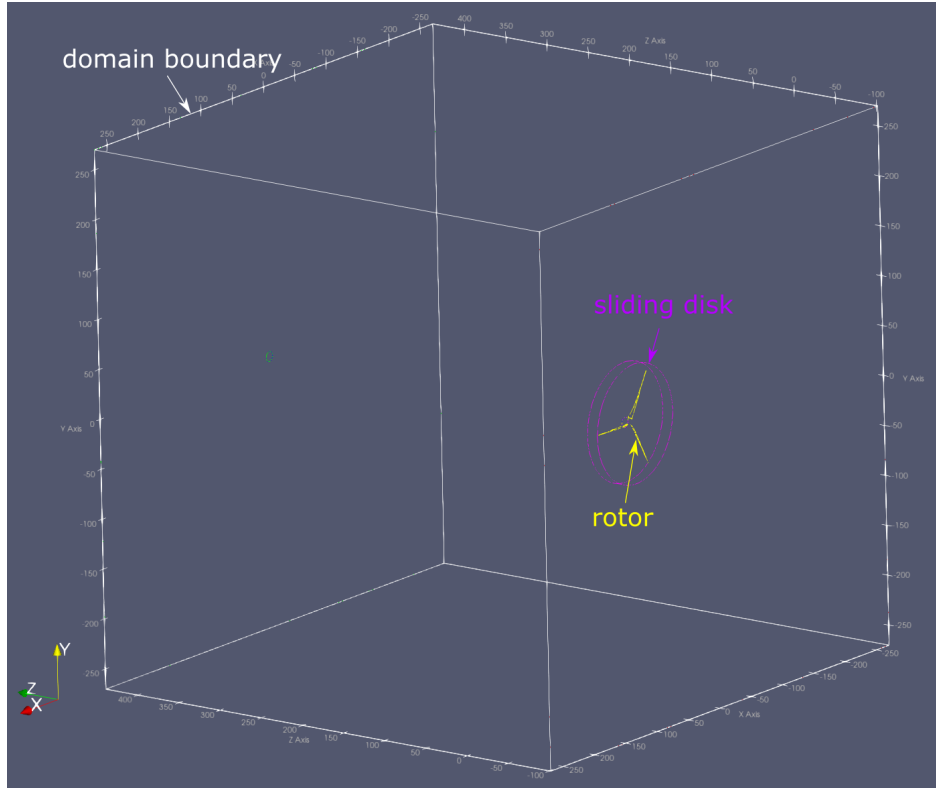


Figure 4.1. CFD computation domain

The aerodynamic noise of the rotor is computed at different locations on the plane of rotation. The result at different distances is shown in Figure 4.2. It is shown that the broadband noise induced by the locally unsteady surface load is mainly within the audible frequency range (>20 Hz), but the level is much lower than the hearing threshold. Therefore, it can be concluded that the broadband aerodynamic noise emitted from a wind turbine does not have a substantial impact. This fact helps to justify the use of TDRIP program in wind turbine noise prediction. In Chapter 1, it is shown that the infrasound emitted from wind turbines has substantial environmental impacts, and the TDRIP program is capable to predict the narrowband infrasound emission of wind turbines.

The wind turbine rotor in TDRIP program is shown in Figure 4.3a, consisting of 19500 quadrilateral elements. Dimensions of the turbine are shown in Table 3.1. Aerodynamic noise of single turbine is computed on virtual microphones at different (R_{mic}, θ_{mic}) locations (Fig. 4.3b). Ground effect is considered in the way introduced in Chapter 3.

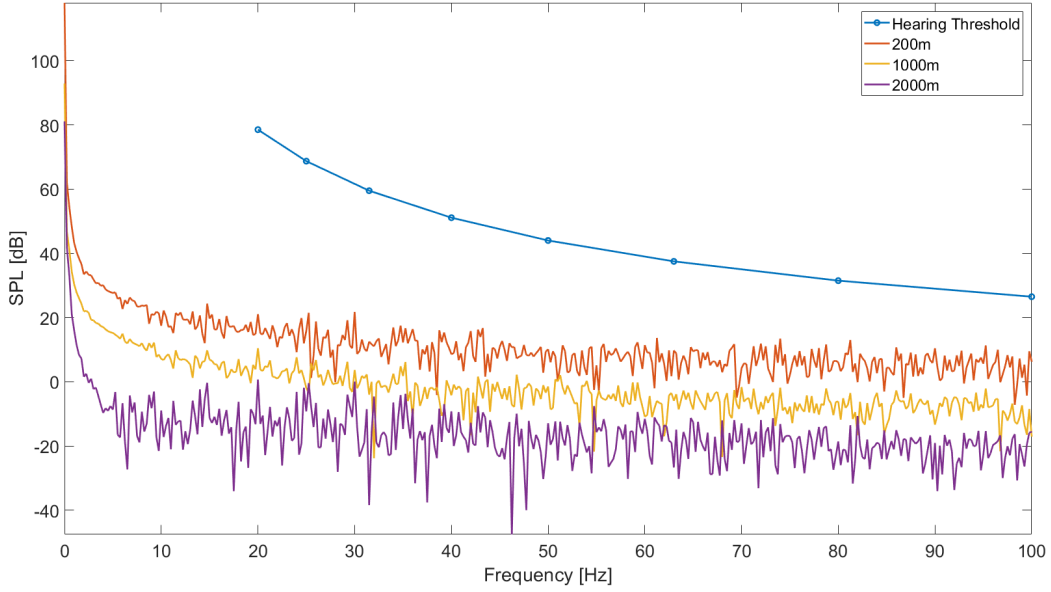


Figure 4.2. Aerodynamic noise computed by CFD

Sound pressure of a few locations is shown in Figure 4.4. The signal is perfectly periodic and only one period of the signal is computed and shown. The number of the blades is 3, therefore BPF is three times the frequency of rotation. Judging by the waveform shown in Figure 4.4, the BPF component is by far the most dominant frequency component of the result. Loading noise result has a DC shift and that can be directly explained by Equation 2.39. The DC component is maximized as θ_{mic} approaches 90° (and 270°), which is on the front and back sides of the rotor. On the contrary, the BPF component and its harmonics are maximized as θ_{mic} approaches 0° (and 180°), which is on the left and sides of the rotor.

Because the signals received by the virtual microphone are periodic, the Fourier coefficient spectrum is computed. Figure 4.5 shows the one-sided spectrum of the signal shown in Figure 4.4. The BPF (0.5 Hz) component is approximately 20 dB greater than its harmonics. Therefore, in the following analysis, higher-order harmonics of BPF component are neglected. It should be noted that the higher-order harmonics indicate the deviation of a waveform from a sinusoidal wave at BPF. The deviation can be a result of the Doppler effect or ground effect. In the case of our study, the Mach number of the blade tip is 0.164, which means the Doppler factor $1/(1 - M_r)$ is between $0.93 \sim 1.08$ on the plane of rotation. When M_r

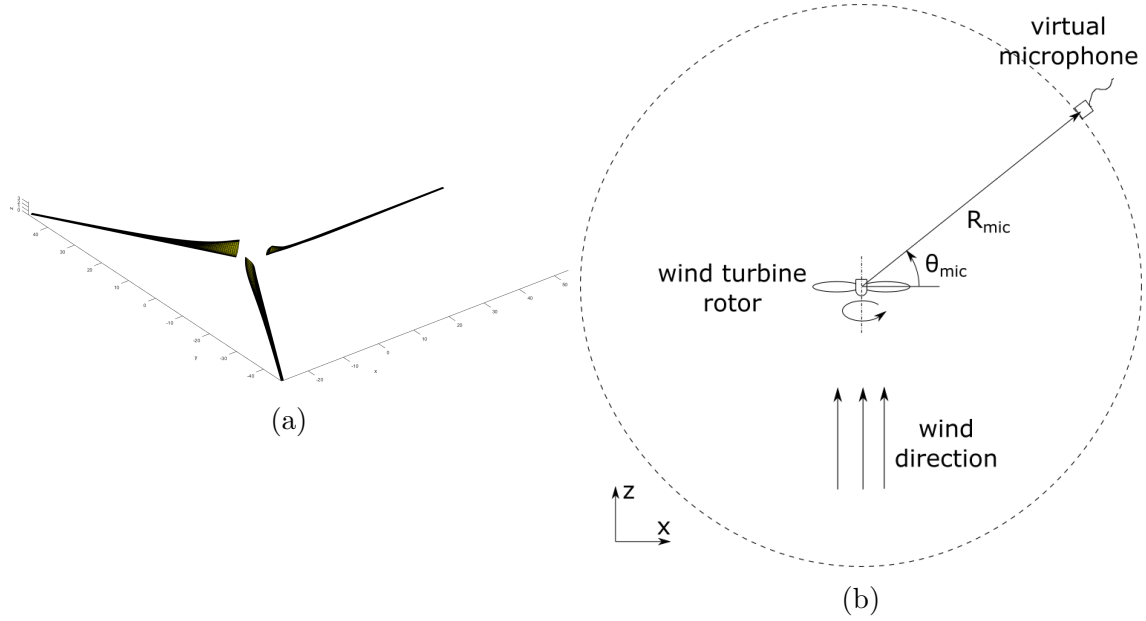


Figure 4.3. (a) Turbine Rotor Element in TDRIP Program and (b) Virtual Microphones

increases, the waveform would deviate more from a sinusoidal wave. The extreme situation is when $M_r = \pm 1$, when discontinuous pressure jump (shock wave) occurs. In that case, more higher-order harmonics could be identified from the Fourier coefficient of the signal. In our study, higher-order harmonics will be neglected because the Doppler effect is weak.

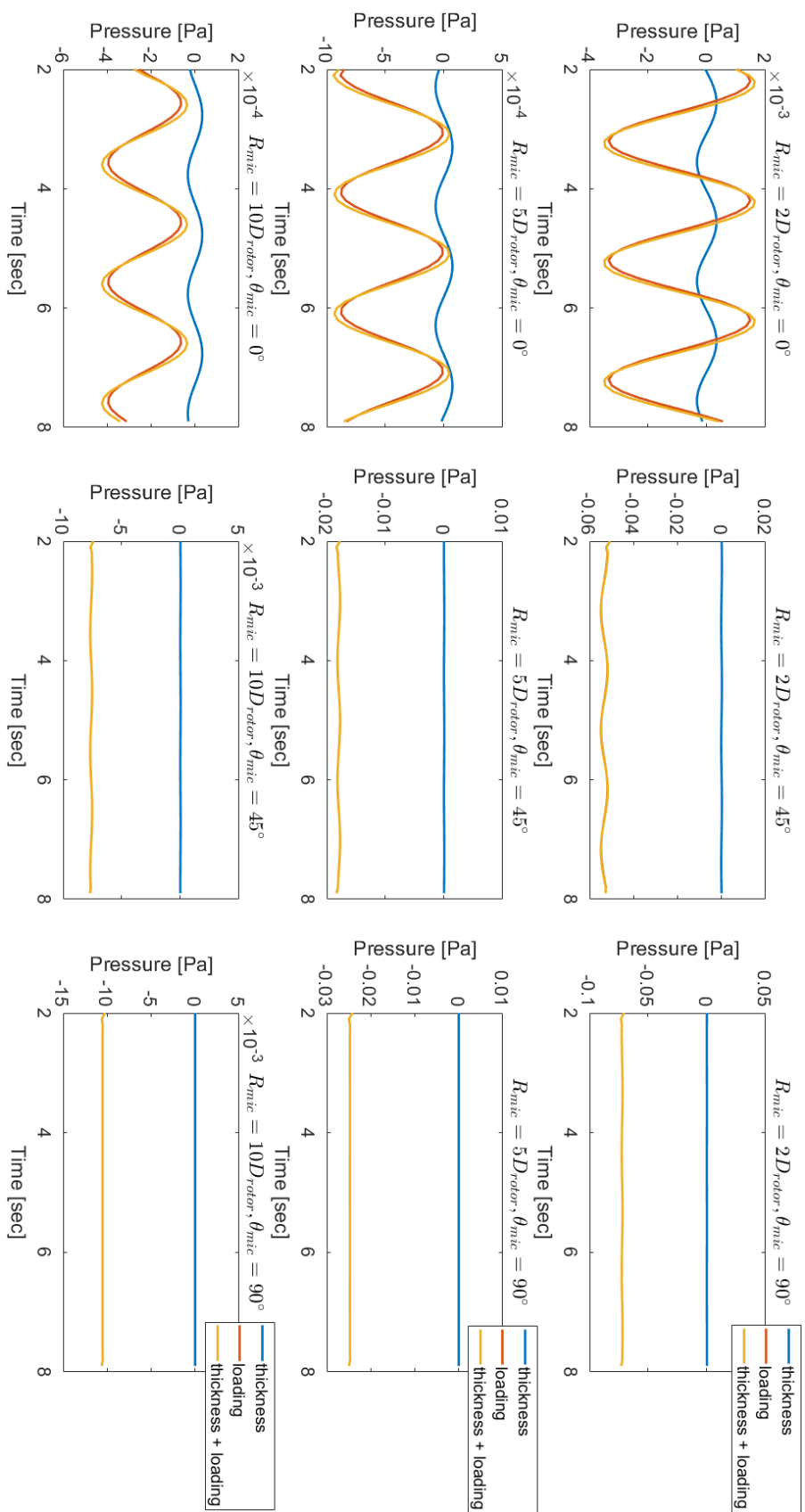


Figure 4.4. Time history of aerodynamic noise at different virtual microphones

In Chapter 2 a misconception was pointed out that Equation 2.38 and 2.39 are not direct evaluations of the sound field of distributed monopoles and dipoles. Instead, the sound can be a mere by-product of motion, as the spectrum shown in 4.5 implies. If the sound field of moving monopoles and dipoles were computed, BPF component would not have been the dominant component. The dominant frequency would have been that of monopole/dipole, and the motion of the source would cause Doppler modulation. The signals shown in Figure 4.4 are analogous to electromagnetic waves induced by constant but moving electric current. Maxwell's equation indicates that either a time-varying or a moving current density induces electromagnetic waves. Signals shown in Figure 4.4 are conceptually similar to electromagnetic waves caused by current densities in a circular motion, and that of acoustic monopoles/dipoles are analogous to electromagnetic waves induced by time-varying electric current density.

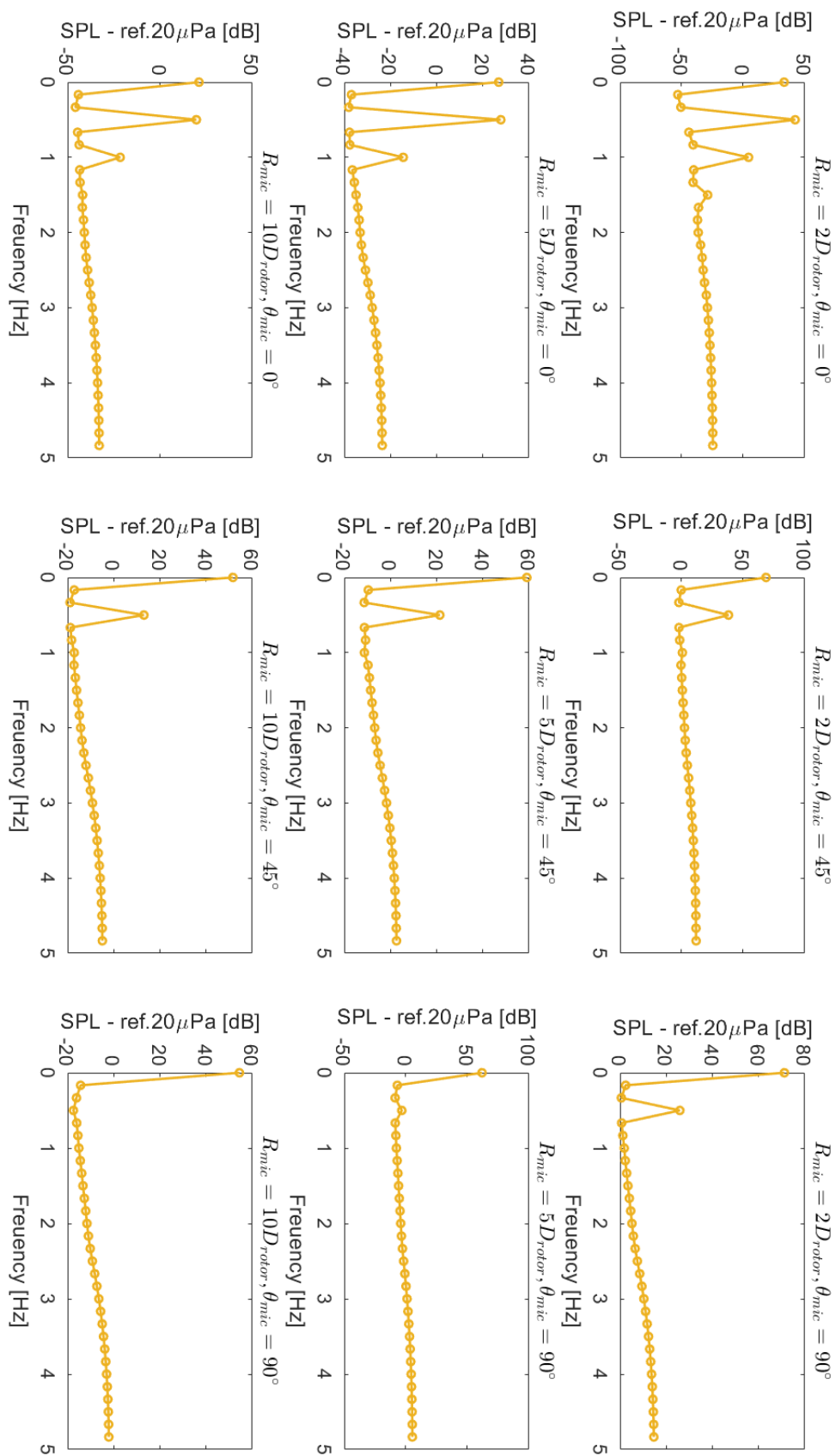


Figure 4.5. Fourier coefficient

Directivity patterns of aerodynamic noise is shown in Figure 4.6. In Figure 4.6, the plane of rotation is aligned with 0° - 180° direction. 270° is the frontal direction and 90° is the rear direction of the rotor. Wind direction is along 90° - 270° direction. The DC component has a directivity of an 8 shape. The two lobes are in 90° - 270° direction. The BPF component has a directivity pattern of horizontal 8 shapes, whose main lobes are in 0° - 180° . This phenomenon implies that the front and back sides of the turbine emit the least amount of infrasound at BPF and the left and right sides emit the most amount of infrasound. This counterintuitive phenomenon is due to variation of Doppler factor $1/(1-M_r)$. M_r is the Mach number of a source moving towards the observer. Apparently, M_r has a large variation when observed in the plane of rotation, while it has a small variation when observed from the front or back side of the rotor. The directivity of thickness(monopole) noise is always symmetric with respect to the plane of rotation, and this phenomenon is the nature of thickness noise. If the surface of the moving object is not perforated, the thickness noise is directly related to the volume of fluid displaced by the moving object. The directivity of loading(dipole) noise is, however, not symmetric with respect to the plane of rotation. The lobes of loading noise are slightly backward leaning. That's because the blade is twisted and the pressure coefficient distribution on blade sections(Fig. 3.3b) is not symmetrical. The directivity of the 2nd BPF harmonic(and higher-order harmonics) is irregular. However, the magnitude of the 2nd harmonic is about 30~40 dB smaller than that of the 1st harmonic. Therefore 2nd and higher-order BPF harmonics are negligible compared to the fundamental component.

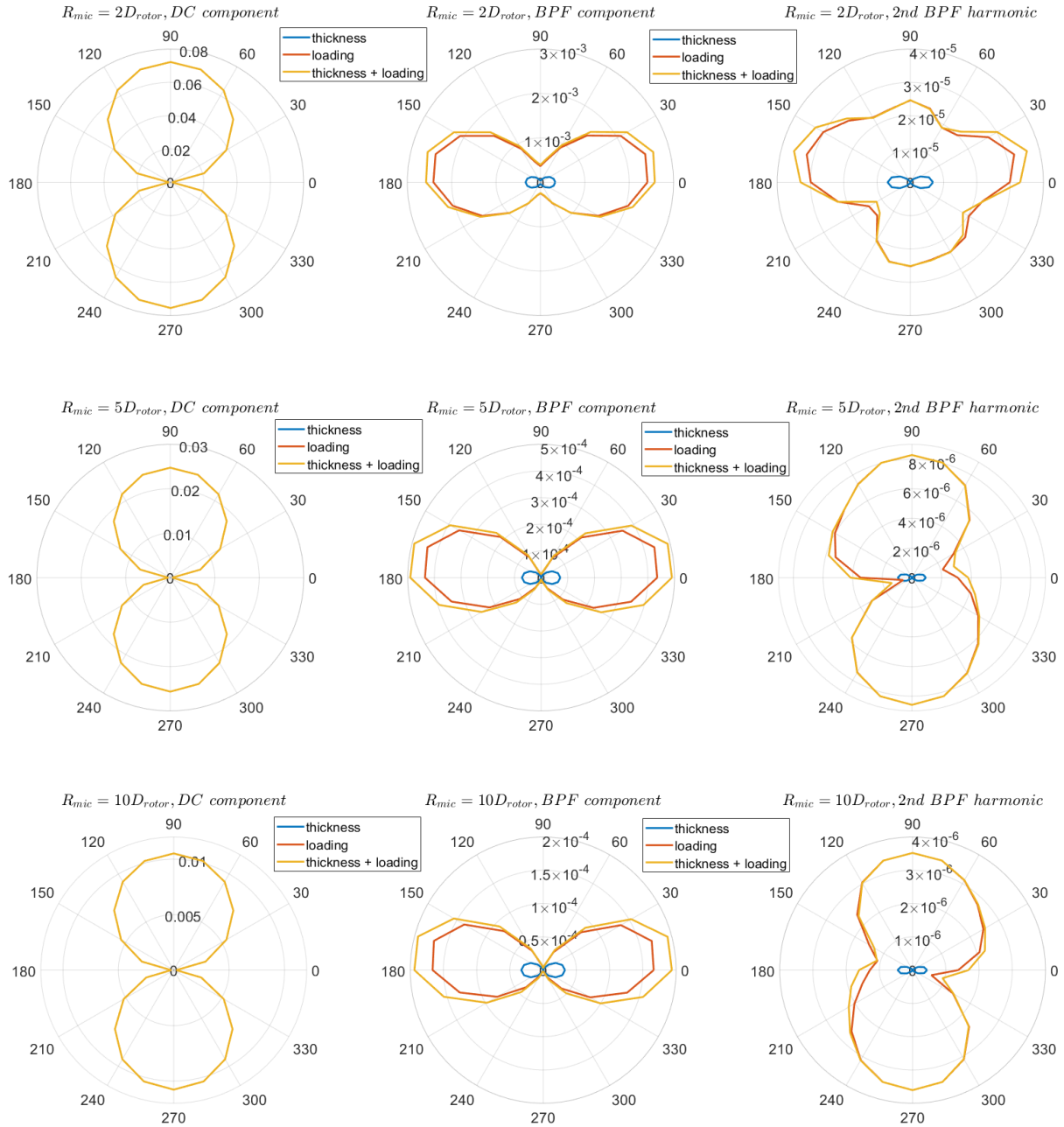


Figure 4.6. Directivity pattern of different frequency components

4.2 Infrasound Emitted from Two Turbines

Multiple wind turbines are usually grouped and operated together as a wind farm. Now that we've investigated the aerodynamic noise of one isolated turbine, it would be of interest to investigate the combined effect of a group of turbines. The aerodynamic noise of two wind

turbines operating at the same time will be investigated. It should be noted that the fluid interaction between the two turbines is not considered.

The configuration of the two turbines is shown in Figure 4.7. Wind direction θ_{wind} is between 0° and 90° . Modern wind turbines have the capability of automatic yaw adjustment so that the turbine always faces the direction of incoming wind. Automatic yaw adjustment is considered in the TDRIP program. $\theta_{wind} = 0^\circ$ is the standard configuration, in which the wake behind wind turbine doesn't affect the other turbine. On the contrary, $\theta_{wind} = 90^\circ$ is when the one turbine is at the center of the wake of the other turbine. The effect of the phase difference of the two turbines is also investigated. Turbine A is phased by φ_d . Because a wind turbine consists of three blades, the effective phase difference only varies between $-60^\circ \sim 60^\circ$.

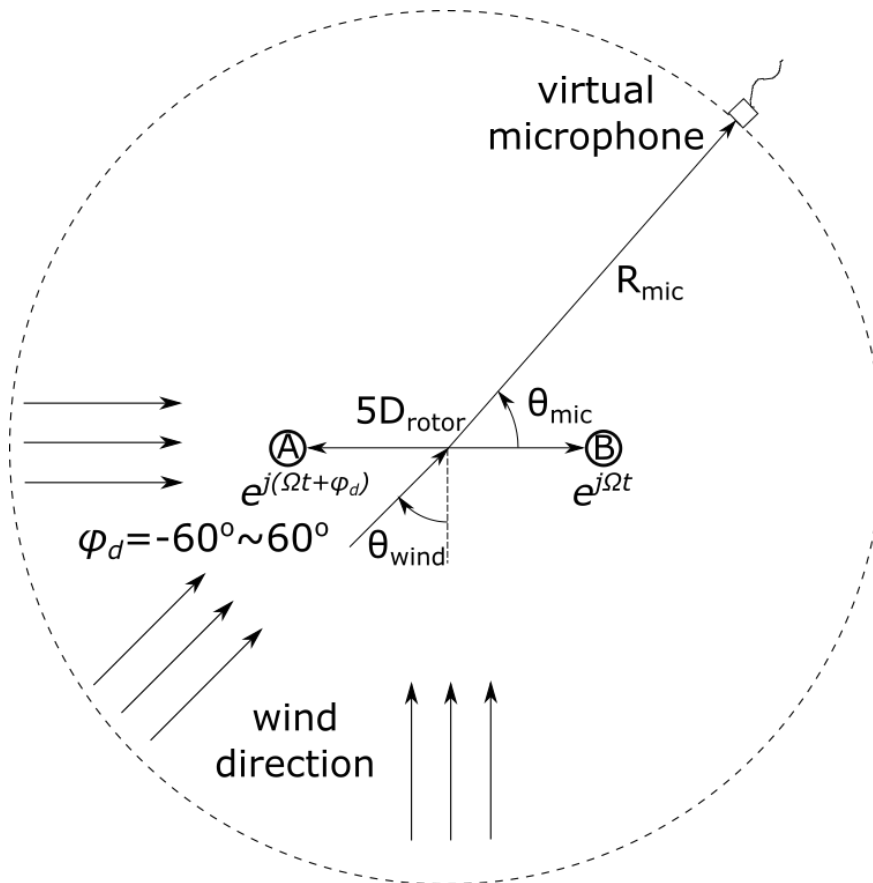


Figure 4.7. Two turbines configuration

4.2.1 Wind direction

The directivity pattern with different wind angles is shown in Figure 4.8. The 8-shape directivity can be seen when the wind is in cardinal direction ($\theta_{wind} = 0^\circ$ and $\theta_{wind} = 90^\circ$), and the main lobes stretch in directions perpendicular to wind directions. When the wind direction is not cardinal, minor lobes exist and the main lobes become smaller. Especially when the wind direction is inter-cardinal ($\theta_{wind} = 45^\circ$), the pattern is an X-shape with 4 lobes of similar sizes.

In general, Figure 4.8 shows that an array of 2 turbines emits significantly less aerodynamic noise in inter-cardinal directions ($\theta_{mic} = 45^\circ, 135^\circ, 225^\circ$ and 315°), no matter in which direction wind comes. This phenomenon is a combined result of both the directivity pattern of a single turbine (Fig. 4.6) and the interference of sound emitted from two turbines. For instance, when $\theta_{wind} = 45^\circ$, due to the 8-shape directivity of single turbine, dips occur on front ($\theta_{mic} = 255^\circ$) and back ($\theta_{mic} = 45^\circ$) sides and lobes occur on left ($\theta_{mic} = 315^\circ$) and right ($\theta_{mic} = 135^\circ$) sides. The dips indeed occur on the front and back sides, but lobes do not occur on the left and right sides. This is because of the cancellation of sound emitted from two turbines. In the case of $\theta_{wind} = 45^\circ$, the difference in distance from turbines to microphones on left and right sides is approximately $\frac{5D_{rotor}}{\sqrt{2}} = 382$ m, which results in a phase difference of 1.11π for BPF component due to time delay. In other words, the sound emitted from two turbines are almost out of phase and cancels each other in certain directions.

This directivity pattern of two turbines with different wind angles is potentially useful in siting of wind turbines based on the noise level. Figure 4.8 implies that in certain directions the array of two turbines always emits less aerodynamic noise than in other directions. Therefore, the siting can be conducted in a way that residential areas are in directions with the least aerodynamic noise emission. Even though only the directivity pattern of two turbines is investigated, the TDRIP program is capable to do the same analysis with tens of wind turbines, and it can be potentially extended to be a wind farm siting optimization tool oriented by aerodynamic noise level reduction.

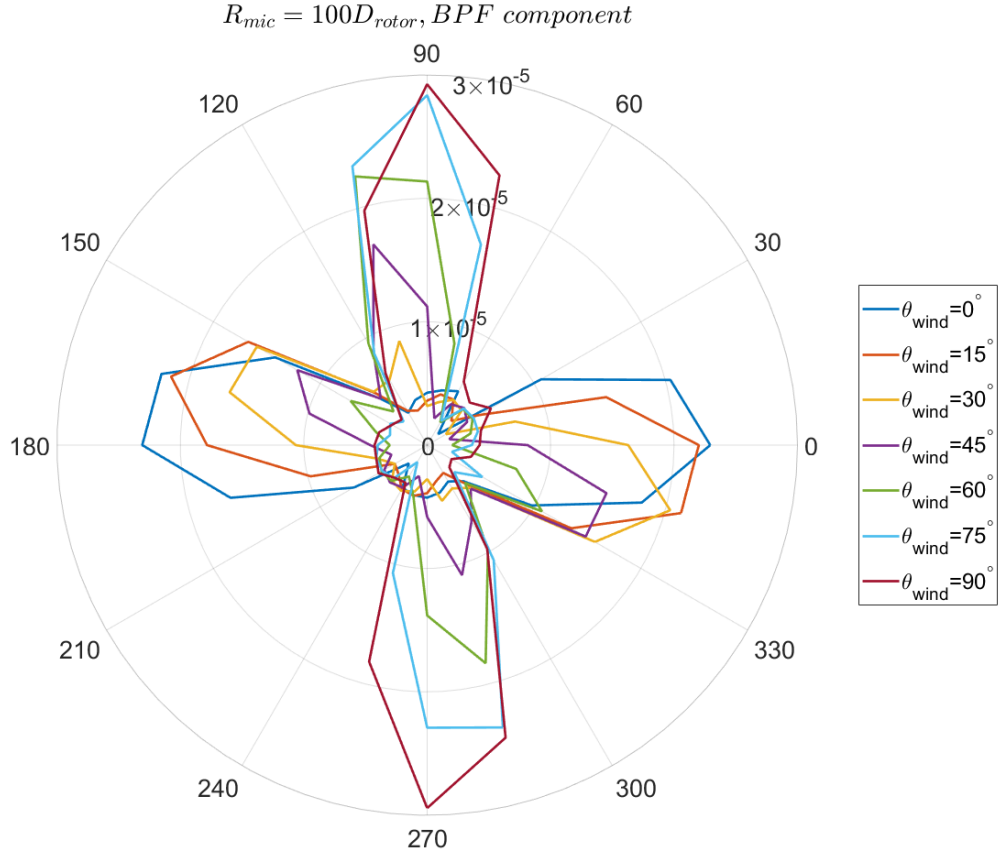


Figure 4.8. Directivity pattern with different wind angle

4.2.2 Phase difference

The directivity pattern with a phase difference is shown in Figure 4.9. For $\varphi_d = 0^\circ$, the directivity is roughly an 8 shape with main lobes stretching in $\theta_{mic} = 0^\circ$ and $\theta_{mic} = 180^\circ$ directions. The two lobes are not symmetric because turbine A is not symmetric to turbine B. When $\varphi_d = \pm 30^\circ$, the aerodynamic noise of two turbines cancel each other on one side and add them together on the other side.

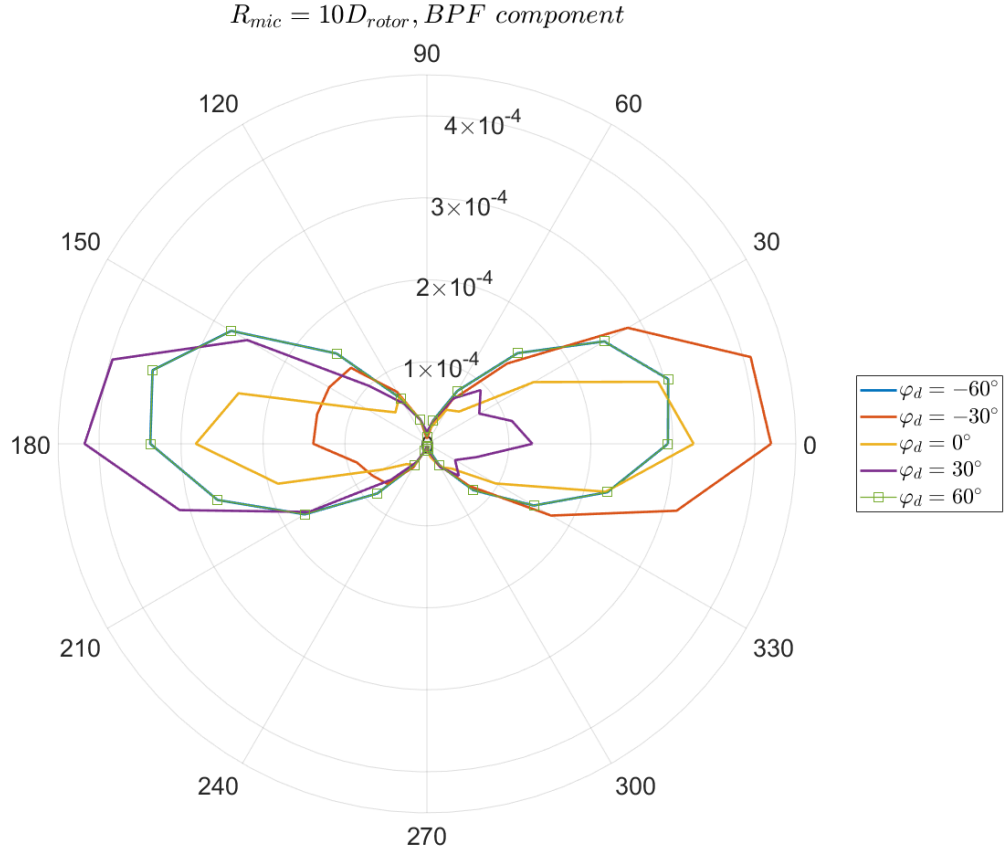


Figure 4.9. Directivity of turbines with phase difference

Figure 4.10 shows time history at $R_{mic} = 10D_{rotor}, \theta_{mic} = 180^\circ$. It can be seen from Figure 4.10a that the two waveforms are almost fully out of phase when $\varphi_d = 30^\circ$ and they are almost fully in phase when $\varphi_d = -30^\circ$. This feature potentially allow us to reduce aerodynamic noise emission in certain directions by adjusting phase differences between turbines.

Effect of phase adjustment is further elaborated in the four turbines configuration shown in Figure 4.11. Assume there is a household in $\theta_{mic} = 15^\circ$ direction and assume rotation of all four turbines are in phase, the level of aerodynamic noise at BPF reaching the household is 26.9 dB. If the phase of turbine A is adjusted to be out of phase with the other three turbines, the level of aerodynamic noise at BPF reaching the household is 21.1 dB. The effect of phase adjustment shown in Figure 4.12 envisions possible wind farm control oriented by noise reduction, using the TDRIP program to estimate noise level.

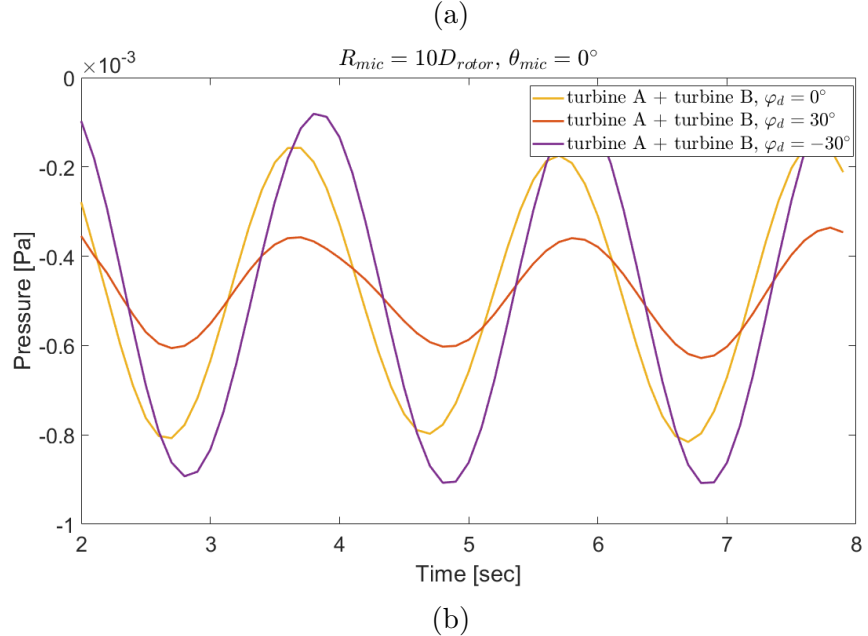
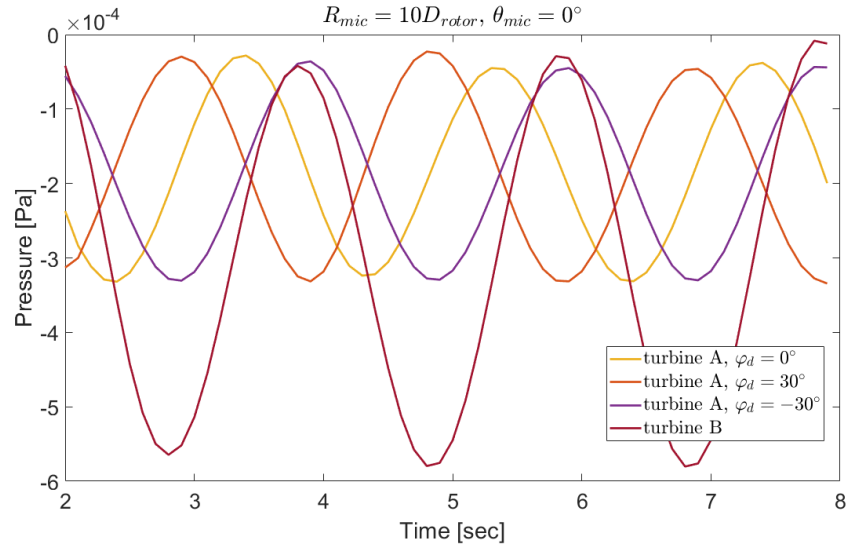


Figure 4.10. Time history of wind turbine infrasound emission with phase difference

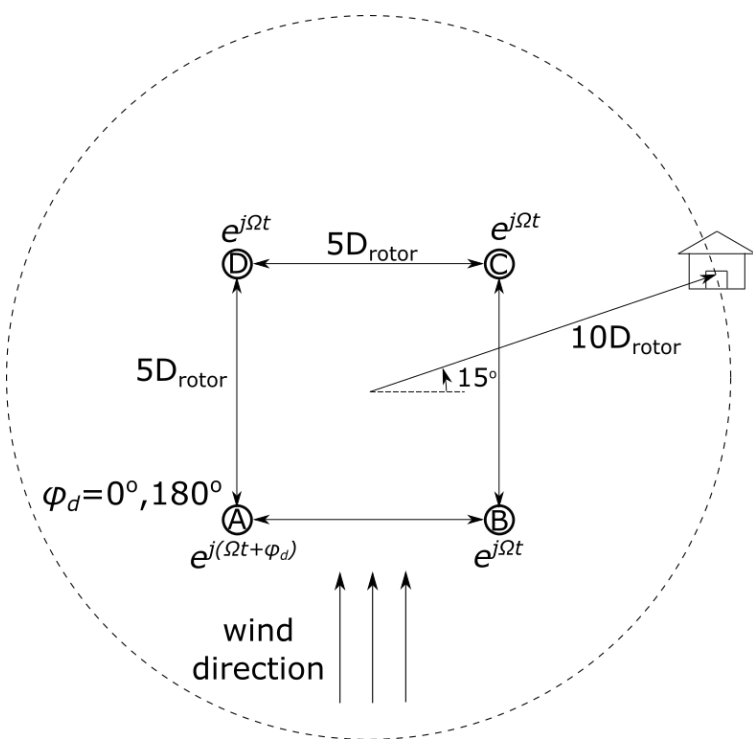


Figure 4.11. Four turbines configuration

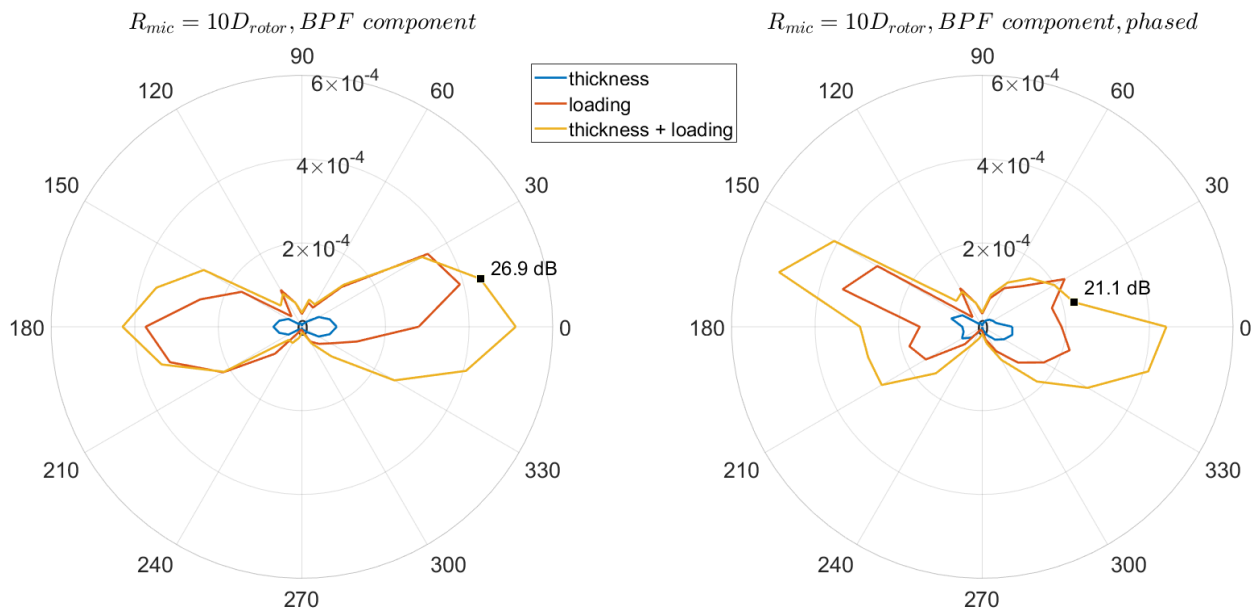


Figure 4.12. Directivity of four turbines

5. SUMMARY AND FUTURE WORK

In the first chapter, the working principles of wind turbines and the development of wind energy were briefly reviewed. The development of wind energy comes with environmental impacts. One of environmental impact, noise, raises public health concerns. People living near wind farms are reported to have so-called *wind turbine syndrome*, and it's likely to be a result of infrasound emitted from wind turbines. In the thesis, this issue is addressed by developing a TDRIP program capable to predict infrasound emission of a group of wind turbines. The TDRIP program is based on acoustic analogy theories that are reviewed in the second chapter. In particular, Farassat's Formulation 1A is implemented in the TDRIP program. Farassat's Formulation 1A is a solution to FW-H equation, and the formulation itself is a surface integral evaluated at retarded emission time. In the third chapter, methods were introduced to numerically evaluate the formulation. The shape of the turbine blade is determined by the basic wind turbine working principles and the surface pressure is determined by using an airfoil analysis tool. Ground effect is taken into account by evaluating the convolution of the incident sound wave and reflection coefficient impulse response. CFD is used to validate the TDRIP program and their results are in good agreement. In the fourth chapter, the aerodynamic noise emitted by a wind turbine rotor is investigated. The spectrum of aerodynamic noise shows that the BPF component is the most significant component. Then the directivity patterns of aerodynamic noise emission of wind turbines are studied. The impact of changing wind direction on aerodynamic noise directivity has been demonstrated. It has also been demonstrated that phase adjustment can effectively reduce aerodynamic noise emission in a certain direction. In summary, the developed TDRIP program is a capable tool to study the aerodynamic noise of wind turbines, and it has the potential to integrate more utilities to aid wind farm siting and control.

5.1 Possible Future Improvement

In this study, only the narrow band infrasound emitted from wind turbine rotors has been studied. However, there are many other mechanisms that can induce noise emission from wind turbines. Therefore, it's desirable to conduct a field experiment to actually measure

wind turbine noise and see the role of the narrow band infrasound compared with other noise. Also, the TDRIP program has only been validated against the CFD simulation result. The experimental result would provide a more solid validation for the TDRIP program.

As described in Chapter 3, the TDRIP program doesn't account for locally unsteady loads, such as turbulence boundary layer, flow instability, or inflow turbulent gust. The TDRIP program can be further developed to include those locally unsteady mechanisms. If the statistics of turbulence are known, it can be simply converted to a time-varying pressure coefficient distribution. Similarly, if the characteristics of instability wave or the correlation of turbulent gust are known, they can be converted to time-varying pressure coefficient distributions that represent locally unsteady loads.

In previous Chapters, a misconception is pointed out that formulation 2.38 and 2.39 are not necessarily sound field solutions of moving monopoles and dipoles. However, the TDRIP program is already modified to compute time domain sound field of moving monopoles and dipoles. Figure 5.1 shows the sound pressure of a rotating monopole/dipole received by a virtual microphone. The frequency of monopole/dipole is 5 Hz and the frequency of rotation is 1 Hz. Sound pressure is directly computed by using equations

$$p_{\text{monopole}}(t) = \left[\frac{j2\pi f \rho Q}{4\pi r(\tau)} \exp(j2\pi f\tau) \right]_{\tau=t-r/c_0}$$

and

$$p_{\text{dipole}}(t) = \left[\frac{j2\pi f D}{r(\tau)} \left(1 + \frac{1}{j2\pi f r(\tau)} \right) \exp(j2\pi f\tau) \cos \theta \right]_{\tau=t-r/c_0},$$

where Q and D are volume flux of monopole and moment of dipole respectively that represent strength of monopole/dipole, θ is the angle between dipole axis and the line joining source and microphone. In Figure 5.1a, it can be clearly seen that the 5 Hz signal is modulated by circular motion of sound source, and the amplitude/frequency modulation is at 1 Hz. It was mentioned that the TDRIP program can be extended to take locally unsteady mechanisms into account. A specific way to achieve that is to convert unsteady mechanisms to a equivalent monopole/dipole distribution and use the program to compute sound field induced by rotating monopoles/dipoles.

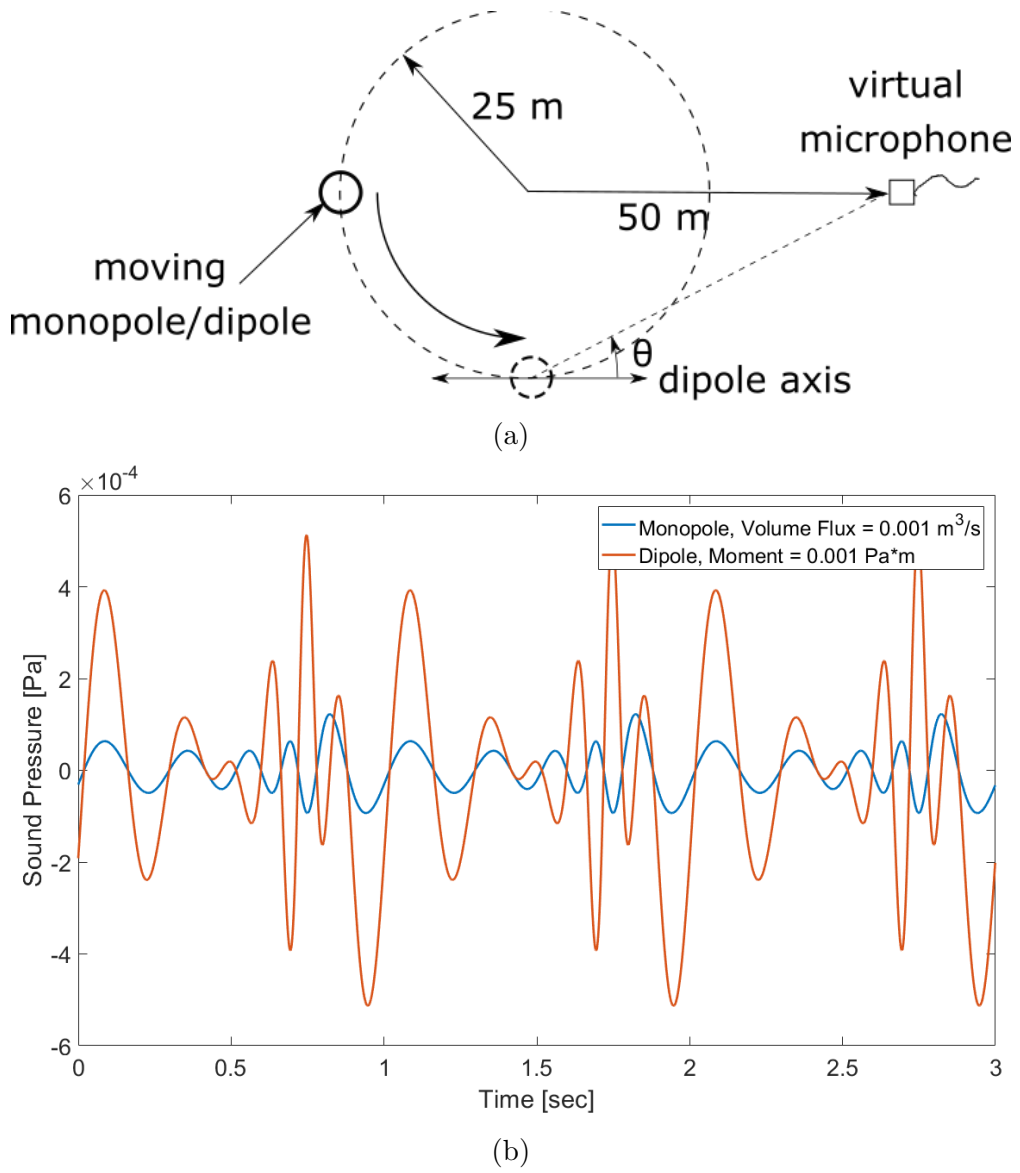


Figure 5.1. (a) Monopole/dipole in circular motion and (b) sound pressure of moving monopole/dipole

It is assumed that wind speed had a uniform profile. However, wind speed usually has a gradient versus altitude, and a non-uniform wind profile affects the angle of attack on different sections of a turbine blade. If the wind profile is known, this effect can be included by tabulating the rotation phase-AOA-pressure coefficient. Each blade section has a certain pressure coefficient distribution at a certain AOA. AOA is related to the altitude of that section, which is a function of the phase of rotation $\Omega\tau$. The wake interaction between wind turbines can be modeled in the same way. The wake of an upwind turbine changes the wind

profile of downwind turbines, and the phase-AOA-pressure coefficient can help us find the pressure coefficient on a certain element at any time.

In Chapter 3, the method to account for the ground effect is introduced. In order to circumvent dealing with non-uniformly sampled signals, by viable region of observers(microphones) has been limited. Only when the observer is placed barely off the ground can the incident signal be uniformly sampled. This assumption is true when the wind turbine is much higher than the observer(microphone). In the future, if wind turbine aerodynamic noise emission towards higher altitude regions is of interest, the signal processing part of the program can be updated so that the convolution of the non-uniformly sampled incident wave and uniformly sampled impulse response can be computed.

In Chapter 4, the effects of wind direction and phase difference on the directivity pattern of a group of turbines are demonstrated. The results envision a wind farm siting tool and a wind farm control strategy based on the aerodynamic noise level in certain directions. In a wind farm, turbines units are sited based on dominant wind direction and the siting criteria is to have the least wake interactions. From Figure 4.8 it can be seen that different wind directions create different directivity patterns. Equivalently, the TDRIP program predicts directivity under different wind farm siting configurations with a dominant wind direction (Fig. 5.2), and that envisions a wind farm siting criteria to control noise level at nearby residential areas. If the wind farm is already built, the TDRIP program can also predict how phase adjustment of turbines can reduce the noise level at a certain location, as demonstrated in Figure 4.12. The capability of the TDRIP program to predict the effect of phase adjustment makes it possible to develop a wind farm control strategy that reduces noise level at certain locations.

The efficiency of TDRIP program can be increased in the future to make it more suitable for applications for larger scales. The requirement of computation resource is linearly dependent on the number of the surface element (Fig. 5.3). The computation time can be further reduced if redundant computation is optimized. The evaluation of formulation involves recursive references of some methods and some values are repetitively computed. The computation can be less repetitive if intermediate results are temporarily stored, and memory can be exchanged for shorter computation time in this way. Additionally, the par-

allel computation will benefit efficiency a lot, because the evaluation of surface integral on one surface element is totally independent of the evaluation on another element.

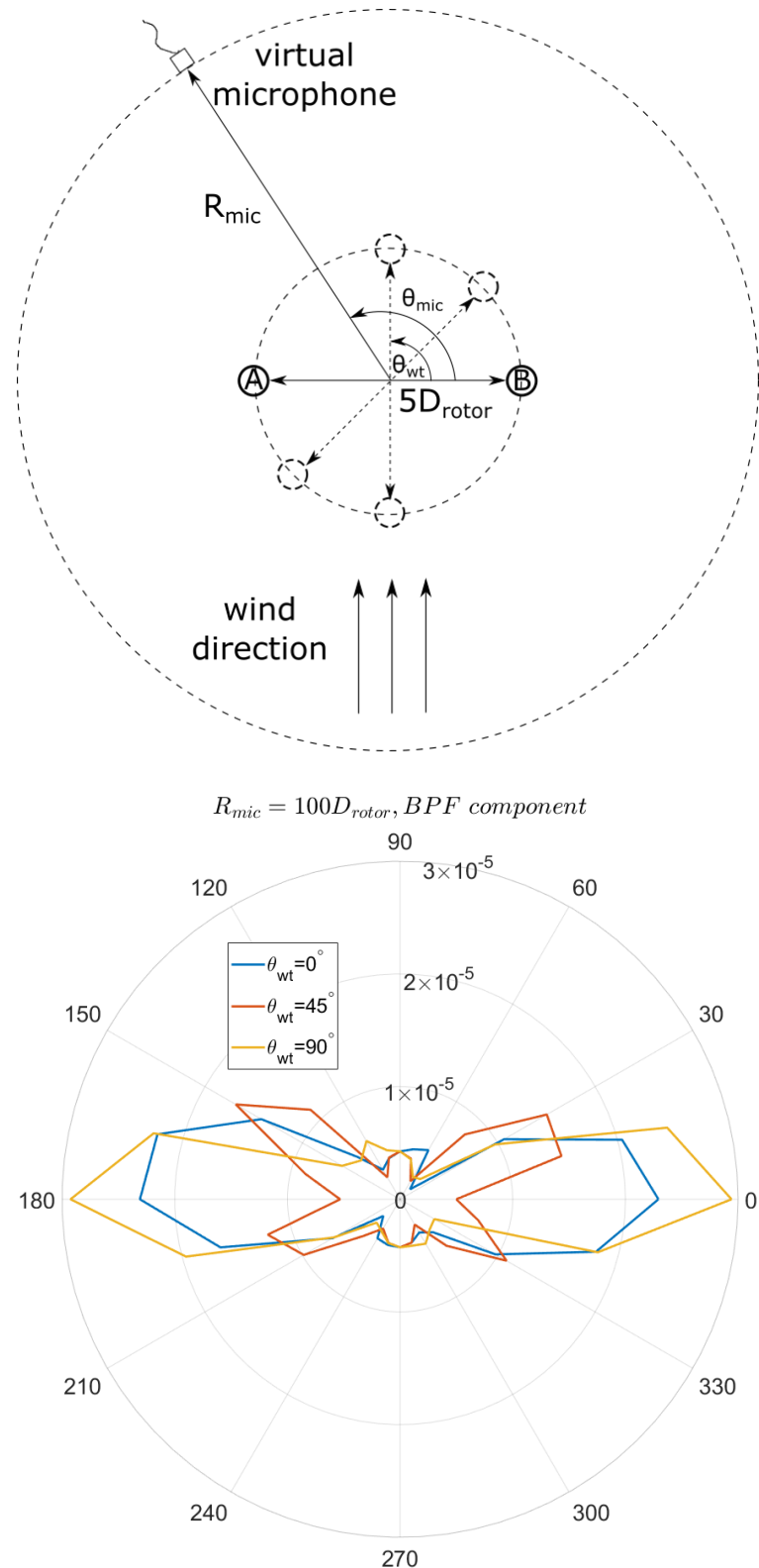


Figure 5.2. Wind turbines siting vs. noise directivity

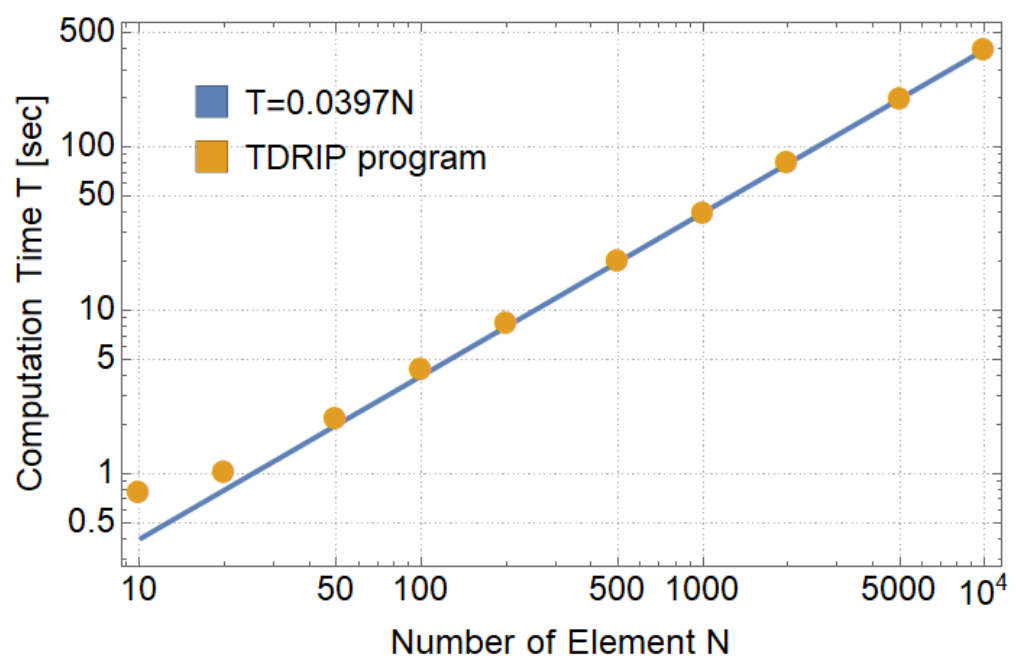


Figure 5.3. Computation time of TDRIP program

REFERENCES

- [1] *Renewable Capacity Statistics 2021*. Abu Dhabi: International Renewable Energy Agency (IRENA), 2021, ISBN: 978-92-9260-342-7.
- [2] [Online]. Available: <https://www.ge.com/renewableenergy/wind-energy>.
- [3] S. Barbarino, W. G. Dettmer, and M. I. Friswell, “Morphing trailing edges with shape memory alloy rods,” *21st International Conference on Adaptive Structures and Technologies (ICAST)*, 2010.
- [4] A. Betz, *Wind-Energie und ihre ausnutzung durch Windmühlen*. Göttingen: Vandenhoeck and Ruprecht, 1926.
- [5] H. Glauert, *The Elements of Aerofoil and Airscrew Theory*, ser. Cambridge Science Classics. Cambridge University Press, 1983. DOI: [10.1017/CBO9780511574481](https://doi.org/10.1017/CBO9780511574481).
- [6] J. F. Manwell, J. G. McGowan, and A. L. Rogers, *Wind Energy Explained: Theory, Design and Application*. Abu Dhabi: John Wiley & Sons, 2009, ISBN: 978-92-9260-342-7.
- [7] T. Knudsen, T. Bak, and M. Svenstrup, “Survey of wind farm control,” *Wind Energy*, vol. 18, pp. 1333–1351, 2015.
- [8] I. Katic and N. O. Jensen, “A simple model for cluster efficiency,” *Proc. Eur. Wind Energy Conf.*, pp. 407–410, 1986.
- [9] P. A. Fleming, P. M. Gebräad, S. Lee, J.-W. van Wingerden, K. Johnson, M. Churchill, J. Michalakes, P. Spalart, and P. Moriarty, “Evaluating techniques for redirecting turbine wakes using sowfa,” *Renewable Energy*, vol. 70, pp. 211–218, 2014. DOI: <https://doi.org/10.1016/j.renene.2014.02.015>.
- [10] J. Annoni, P. Seiler, K. Johnson, P. Fleming, and P. Gebräad, “Evaluating wake models for wind farm control,” *2014 American Control Conference*, pp. 2517–2523, 2014. DOI: [10.1109/ACC.2014.6858970](https://doi.org/10.1109/ACC.2014.6858970).
- [11] National Wind Coordinating Committee (NWCC), *Wind turbine interactions with birds, bats, and their habitats: A summary of research results and priority questions*, 2010.
- [12] R. D. Jeffery, C. Krogh, and B. Horner, “Adverse health effects of industrial wind turbines,” *Can. Fam. Physician*, vol. 59, pp. 473–475, 2013.
- [13] Massachusetts Department of Environmental Protection, “Wind turbine health impact study: Report of independent expert panel,” 2012.

- [14] J. H. Schmidt and M. Klokker, “Health effects related to wind turbine noise exposure: A systematic review,” *PLoS ONE*, vol. 9(12), 2014. doi: [10.1371/journal.pone.0114183](https://doi.org/10.1371/journal.pone.0114183).
- [15] E. Dommes, H. C. Bauknecht, G. Scholz, Y. Rothemund, J. Hensel, and R. Klingebiel, “Auditory cortex stimulation by low-frequency tones—an fmri study,” *Brain Research*, vol. 1304, pp. 129–137, 2009. doi: [10.1016/j.brainres.2009.09.089](https://doi.org/10.1016/j.brainres.2009.09.089).
- [16] F. van den Berg, “Wind turbine noise: An overview of acoustical performance and effects on residents,” *Annual Conference of the Australian Acoustical Society 2013, Acoustics 2013: Science, Technology and Amenity*, pp. 471–477, 2013.
- [17] D. G. Stephens, K. P. Shepherd, H. H. Hubbard, and F. W. Grosveld, “Guide to the evaluation of human exposure to noise from large wind turbines,” 1982, NASA/TM-83288.
- [18] N. Pierpont, “Wind turbine syndrome,” 2006, Testimony before the New York State Legislature Energy Committee.
- [19] G. W. Kamperman and R. R. James, “Simple guidelines for siting wind turbines to prevent health risks,” *Proceedings NoiseCon 2008*, 2008.
- [20] G. P. van den Berg, “The beat is getting stronger: The effect of atmospheric stability on low frequency modulated sound of wind turbines,” *Journal of Low Frequency Noise, Vibration and Active Control*, vol. 24(1), pp. 1–24, 2005.
- [21] L. Gutin, “On the sound field of a rotating propeller,” 1948, NACA/TM-1195.
- [22] M. J. Lighthill, “On sound generated aerodynamically. i. general theory,” *Proc. R. Soc. Lond. A Math. Phys. Sci.*, vol. 211, pp. 564–587, 1952.
- [23] N. Curle, “The influence of solid boundaries upon aerodynamic sound,” *Proc. R. Soc. Lond. A Math. Phys. Sci.*, vol. 231, pp. 504–514, 1955.
- [24] J. E. Ffowcs Williams and D. L. Hawkings, “Sound generation by turbulence and surfaces in arbitrary motion,” *Phil. Trans. R. Soc. Lond. A Math. Phys. Sci.*, vol. 264, pp. 321–342, 1969.
- [25] F. Farassat and G. P. Succi, “A review of propeller discrete frequency noise prediction technology with emphasis on two current methods for time domain calculations,” *Journal of Sound and Vibration*, vol. 71(3), pp. 399–419, 1980.
- [26] F. Farassat, “Linear acoustic formulas for calculation of rotating blade noise,” *AIAA Journal*, vol. 19(9), pp. 1122–1130, 1981.

- [27] F. Farassat, “Derivation of formulations 1 and 1a of farassat,” 2007, NASA/TM-2007-214853.
- [28] J. N. Pinder, “Mechanical noise from wind turbine,” *Wind Engineering*, vol. 16(3), pp. 158–168, 1992.
- [29] S. Wagner, R. Bareib, and G. Guidati, *Wind Turbine Noise*. Berlin: Springer, 1996, ISBN: 978-3-642-88712-3.
- [30] S. B. Pope, *Turbulent Flows*. Cambridge: Cambridge University Press, 2000, ISBN: 978-0-511-84053-1.
- [31] N. H. Kemp and W. R. Sears, “The unsteady forces due to viscous wakes in turbomachines,” *Journal of the Aeronautical Sciences*, vol. 22(7), pp. 478–483, 1955.
- [32] M. S. Howe, *Theory of Vortex Sound*. Cambridge: Cambridge University Press, 2002, ISBN: 978-0-511-75549-1.
- [33] J. E. Ffowcs Williams and L. H. Hall, “Aerodynamic sound generation by turbulent flow in the vicinity of a scattered half plane,” *Journal of Fluid Mechanics*, vol. 40(4), pp. 657–670, 1970.
- [34] R. K. Amiet, “Noise due to turbulent flow past a trailing edge,” *Journal of Sound and Vibration*, vol. 47(3), pp. 387–393, 1976.
- [35] R. W. Paterson, R. K. Amiet, and C. L. Munch, “Isolated airfoil-tip vortex interaction noise,” *Journal of Aircraft*, vol. 12(1), pp. 34–40, 1975.
- [36] F. Farassat, “Theory of noise generation from moving bodies with an application to helicopter rotors,” 1975, NASA Technical Report R-451.
- [37] K. S. Brentner, “An efficient and robust method for predicting helicopter high-speed impulsive noise,” *Journal of Sound and Vibration*, vol. 203(1), pp. 87–100, 1997.
- [38] J. Casper, “A new time domain formulation for broadband noise predictions,” *International Journal of Aeroacoustics*, vol. 1(3), pp. 207–240, 2002.
- [39] F. Farassat, “Theoretical analysis of linearized acoustics and aerodynamics of advanced supersonic propellers,” pp. 1–15, 1985, AGARD-CP-366 (10).
- [40] T. F. Brook, D. S. Pope, and M. A. Marcolini, “Airfoil self-noise and prediction,” 1985, NASA Reference Publication 1218.

- [41] S. Oerlemans and J. G. Schepers, “Prediction of wind turbine noise and validation against experiment,” *International Journal of Aeroacoustics*, vol. 8(6), pp. 555–584, 2009.
- [42] O. Marsden, C. Bogey, and C. Bailly, “Direct noise computation around a 3-d naca 0012 airfoil,” 12th AIAA/CEAS Aeroacoustics Conference (27th AIAA Aeroacoustics Conference). DOI: [10.2514/6.2006-2503](https://doi.org/10.2514/6.2006-2503).
- [43] J. Chicheportiche and X. Gloerfelt, “Direct noise computation of the flow over cylindrical cavities,” 16th AIAA/CEAS Aeroacoustics Conference. DOI: [10.2514/6.2010-3775](https://doi.org/10.2514/6.2010-3775).
- [44] M. E. Goldstein, “A generalized acoustic analogy,” *Journal of Fluid Mechanics*, vol. 48, pp. 315–333, 2003. DOI: [10.1017/S0022112003004890](https://doi.org/10.1017/S0022112003004890).
- [45] K. Attenborough, “Acoustical impedance models for outdoor ground surfaces,” *Journal of Sound and Vibration*, vol. 99, no. 4, pp. 521–544, 1985. DOI: [https://doi.org/10.1016/0022-460X\(85\)90538-3](https://doi.org/10.1016/0022-460X(85)90538-3).
- [46] D. M. Somers, “S816, S817, and S818 Airfoils,” 2004. DOI: [10.2172/15011674](https://doi.org/10.2172/15011674).
- [47] M. M. Hand, D. A. Simms, L. J. Fingersh, D. W. Jager, J. R. Cotrell, S. Schreck, and S. M. Larwood, “Unsteady aerodynamics experiment phase vi: Wind tunnel test configurations and available data campaigns,” 2001. DOI: [10.2172/15000240](https://doi.org/10.2172/15000240).
- [48] [Online]. Available: <http://www.xflr5.tech/>.
- [49] A. Epikhin, I. Evdokimov, M. Kravoshin, M. Kalugin, and S. Strijhak, “Development of a dynamic library for computational aeroacoustics applications using the openfoam open source package,” *Procedia Computer Science*, vol. 66, pp. 150–157, 2015. DOI: <https://doi.org/10.1016/j.procs.2015.11.018>.
- [50] [Online]. Available: <https://github.com/unicfdlab/libAcoustics/tree/digitef-dev-2012>.